**Title**
Terahertz Imaging and Remote Sensing Design for Applications in Medical Imaging



**Author**
Sung, Shijun

**Publication Date**
2013

Peer reviewed|Thesis/dissertation

UNIVERSITY OF CALIFORNIA

Los Angeles

# Terahertz Imaging and Remote Sensing Design for Applications in Medical Imaging

A thesis submitted in partial satisfaction

of the requirements for the degree Master of Science

in Electrical Engineering

by

Shijun Sung

2013

ABSTRACT OF THE THESIS

Terahertz Imaging and Remote Sensing Design for Applications in Medical Imaging

by

Shijun Sung

Master of Science in Electrical Engineering

University of California, Los Angeles, 2013

Professor Warren S. Grundfest, Chair

THz region (1 mm – 0.1 mm, or 300 GHz and 3 THz) of the electromagnetic spectrum attracts applications in medical imaging, with its high dielectric constant of water, low non-ionizing photon energy (0.4-40 meV), and robustness against scattering from rough surface interface. This study investigates THz optical imaging system design and engineering, and explores implementation of THz imaging method for application in remote sensing of physiological tissue. Specifically, the focus of this manuscript is to explore two important topics in remote sensing design, with analysis of quasi-optical systems design and effect of rough surface scattering in THz wavelength.

An overview of THz imaging field and application to medical imaging are presented. A survey of current methods THz imaging and remote sensing scheme is made to provide context for system design consideration. As an example, the direct-detection THz imaging system is characterized, and used in experiments for the following sections.

In the second section, a detailed analysis of commonly used quasi-optical component (off-axis parabolic mirrors) is performed to investigate its focusing properties at THz wavelength. Additional attention is directed to polarization aberration effect in the propagation of coherent, linearly polarized THz beam through series of mirrors.

The third section applies Kirchhoff random rough surface scattering theory at THz region, and provides analysis of signal strength and variance in the signal-to-noise ratio (SNR) in imaging.

Lastly, a beam-scanning imaging system is constructed and demonstrated as an effort toward practical clinical application. The system employs a spinning polygon mirror and Michelson interferometer based design to allow source, detector, and target to remain fixed and perform imaging at a dramatically faster speed. The system achieves a focused THz beam diameter of 1.66mm and a large depth of field of >25 mm, and acquisition speed of minimum 100 pixels/s. Images of characterization targets and *ex vivo* tissue samples are presented.

The thesis of Shijun Sung is approved.

Oscar M. Stafsudd

Benjamin S. Williams

Warren S. Grundfest, Committee Chair

University of California, Los Angeles

2013

# Table of Contents

# List of Figures and Tables

## Figures

## Tables

# Chapter 1 Introduction and background

## 1.1. Properties of THz Region and Applications in Medical Imaging

Terahertz (THz) frequency band spans the sub-millimeter (1 mm – 0.1 mm) region of the electromagnetic spectrum with frequencies between 300 GHz and 3 THz [1]. The THz region has been considered as the least studied frequency band due to challenges in generating and detecting THz frequencies. Advancements and innovations in THz source and detector devices have allowed THz science and technology to become expanding areas of research and systems in the past few decades. Potential application of THz frequencies are research interests in many fields, including but not limited to radioastromony, atmospheric science, security applications in screening and illicit material detection, non-destructive evaluation (NDE), communications technology, biological and medical sciences, and spectroscopy [1, 2].

THz frequencies possess properties that are of particular interest in medical imaging. Corresponding to the rotational and vibrational resonance of $H_2O$, THz frequency readily interacts with water in vapor phase. The high dielectric constant of liquid water at THz frequencies provides high sensitivity to hydration [3-7] in biological tissue. Such sensitivity can be used to precisely sense tissue hydration in a point measurement, or generate contrast in THz signal to spatially resolve tissue hydration in an image. Coupled with the low loss properties of typical tissue constituents, THz imaging facilitates accurate, high dynamic range detection of slight variations in the water content of tissue. THz sensing of biological tissue also benefits from its long wavelength, characterized by low, non-ionizing photon energy (0.4-40 meV), less severe scattering from the rough tissue interfaces, high sensitivity to polar molecules, the ability to penetrate through clothing, and synthetics. These properties make THz imaging a potentially ideal tool for

in-vivo detection and monitoring of skin surface abnormalities, burns, scars, wounds, and skin cancer [6, 8]. Variations in dielectric function due to hydration have been measured in a range of tissue types and pathologies, including skin burns [7, 9, 10].

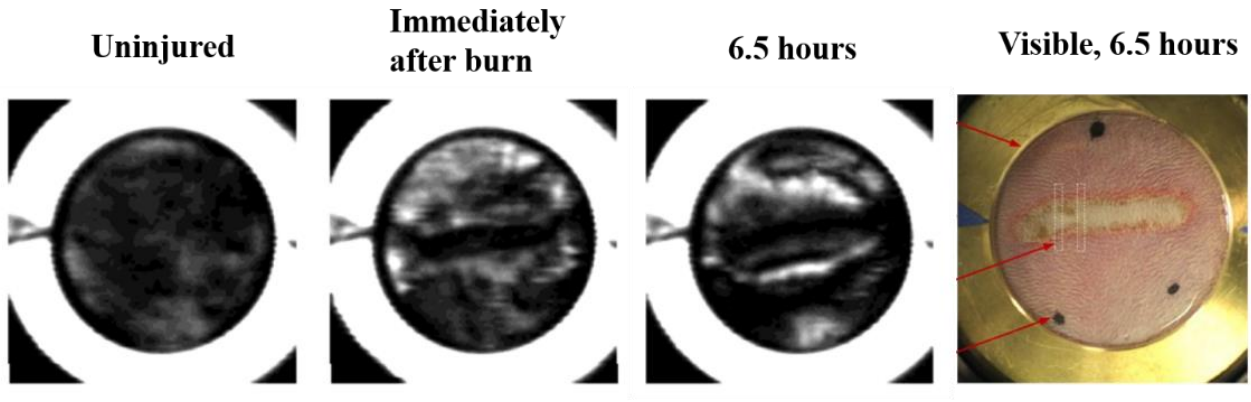


Figure 1-1 THz images of burn wound in in-vivo rat model [11]

Terahertz imaging systems have been developed and implemented in a number of fields for both research and commercial applications including NDE, security imaging, and medical imaging. THz medical imaging has been applied for the detection of skin cancer[12, 13], burn wound diagnosis [4, 14, 15], and corneal hydration sensing [3, 16]. *In vivo* burn studies have shown promising capabilities of THz hydration imaging for the accurate and non-invasive characterization of burn wound severity within 1 hour post burn injury as well as clinical utility for bedside care.

Human tissues vary in structure and composition based on their functions, location, and exposure to different environmental conditions. However, almost all soft tissue is predominantly composed of water: mean epidermal skin is 70% water by weight; cornea under normal condition is 78% water, and liver is 70% water. Given high THz absorption of water and the predominant presence

of water in physiological tissue, reflective THz imaging has distinct advantages over earlier transmission-based systems, and likely the only option for *in vivo* applications.

The field of medical imaging has experienced significant increases in research activity and efforts towards the implementation of a clinically viable instrument [7, 8]. In order to apply improvements in THz science and device engineering for high-impact, practical medical applications, it is crucial to understand how THz radiation interacts with optical devices and components, and with physiological medium.

### 1.2. Room-temperature detector components in THz region

Development of THz detectors, especially for room-temperature operation, posed challenges from both photonics and electronics fronts. The photon energy ($h\nu$) in the THz region is much less than $k_BT$ of room temperature (0.0256 eV), hence atomic and molecular transitions cannot be used for detection at room temperature since quantized states separated by $h\nu$ at THz frequency tend to have the same populations. [17] In electronic detection, THz frequencies are too fast for free carriers to respond in semiconductor devices. For example, in Drude AC conductivity model (equation 1), THz frequencies give $\omega\tau>>1$ and the electromagnetic wave energy to the device is significantly hindered. [17]

$$\sigma = \frac{\sigma_0}{1 + j\omega\tau} \quad (1)$$

#### 1.2.1. Room Temperature THz Detectors

Room-temperature detection is strongly desirable in practical application of THz engineering in medical imaging and bedside devices. Typical room-temperature calorimetric terahertz detectors, such as pyroelectric detectors, microbolometers or Golay cell detectors, measure the heating of a substance that changes properties as a function of temperature change. Microbolometers are

uncooled thermal sensors that change resistance by change in temperature and can be fabricated in arrays to realize a focal plane staring array. [18] However, the response time of the microbolometers and Golay cells are close to DC, and therefore cannot be used in pulsed operation. Fast charge transport between the metal-semiconductor junctions also allow room-temperature detection of THz frequency. Schottky-diode detectors have been historically employed in direct detection of millimeter and submillimeter wavelengths at large video bandwidth owing to their short response time [18]. Advancement in diode design to have low forward turn-on voltage allows for zero-bias operations to achieve ultralow noise, high sensitivity, and larger bandwidth. [18, 19] Two detection schemes are introduced for THz imaging system implementation in medical imaging settings.

1.2.2. THz Time-domain System

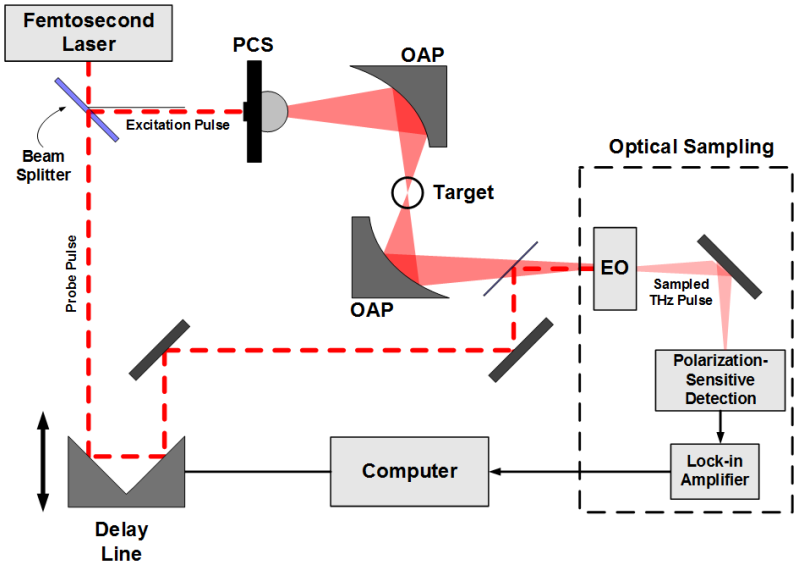


Figure 1-2. Block-diagram of a typical THz time-domain system with an electro-optical sampling (EOS) set-up.

THz time-domain spectroscopy (TDS) techniques utilize ultrafast optoelectronics to generate and detect pulsed THz radiation. [20] In a typical TDS set-up, a photoconductive switch driven by

femtosecond (fs) laser excitation generates broadband pulses in the ultrafast substrate extending to THz bandwidth. The current is coupled to planar antenna and consequently to free-space with a hyper-hemispherical silicon lens. [20] Such a device is also sometimes referred to as the Auston switch. THz pulses are re-directed and focused onto a target using a pair of gold or aluminum coated off-axis parabolic mirrors, and either transmitted or reflected from the target. Time-domain analysis performs sampling of the reflected beam by electro-optic crystal or a photoconductive switch identical to the transmitter, to measure amplitude and the phase of the THz pulses. A TDS system employing electro-optical sampling (EOS) configuration is shown in Figure 1-2. [1] The EOS set-up samples the incident THz pulse when the laser probe pulse split from the initial fs laser is passed through the electro-optic crystal via Pockels effect. By mechanically tuning the optical delay line, the THz pulse waveform is optically sampled at a different transient point from each repeated pulse, and the pulse shape can be traced.

From the measurement of the electric field of THz pulses, both real and imaginary components of the dielectric function can be computed via Fourier-transform, provided that the time-domain pulse shaped is traced with sufficient resolution and period [20]. TDS is a powerful technique to study the rich information contained in the resolved THz spectra of the target. [20] Image contrast can be generated directly from the time domain signal or the Fourier transform of the pulse can be computed and show contrast from spectral content. However, each pixel measurement requires fully resolved sampling of THz pulses. While the time-domain system can achieve high SNR [1, 20], it takes up to minutes to acquire a full THz waveform. In imaging applications, acquisition time per pixel is significantly limited by the number of data points and the sweeping speed of the motorized delay line. Medical THz imaging applications demand a sufficient contrast for the target of interest, while affording practical image acquisition time and technique. In the study of

diagnostic imaging of burn wounds, it is hypothesized that the signal contrast arises from tissue water content [3], and can be correlated to tissue damage extent and viability. Sensitive detection of the water may be achieved by aggregate reflected power from the target, rather than measurements of the entire spectrum using time-domain techniques.

1.2.3. Direct Detection System

Although there are different reported values of the complex dielectric constant of liquid water ε at THz regions, both real and imaginary component of $\varepsilon_{water,liquid}$ show large, monotonically decreasing magnitude over the 0.1 THz to 1 THz region. [14, 21]. Figure 1-3 plots ε' and ε" computed from the Double Debye relaxation model [21] at room temperature, which fits well with experimental data measured by Ronne et al [22].

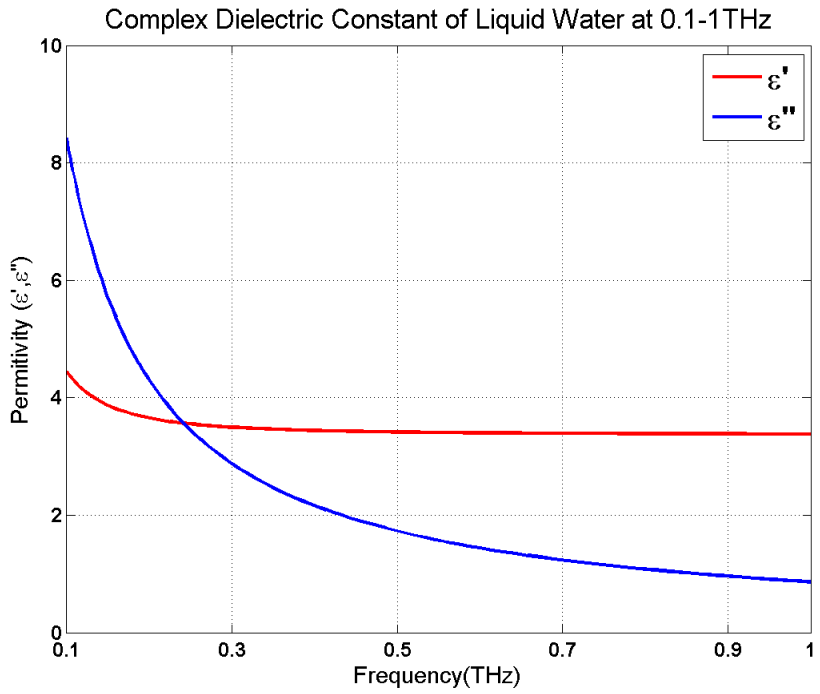


Figure 1-3. Complex dielectric constant of liquid water at room temperature, at 0.1-1THz, computed by Double Debye relaxation model

In physiological tissue, high water content appears to dominate over any possibly distinct features of other compounds, such as polar proteins [14]. The lack of spectral features indicate that the spectrum resolving data acquired in THz TDS may not be all necessary in the bulk physiological measurement. In the application end, clinicians need medical imaging modality that can clearly distinguish diseased tissue from normal tissue and such contrast generation is the principal aim, rather than resolving spectral features. Therefore, for imaging and sensing applications that aim to generate contrast in hydrated tissues, aggregate measurements of the dielectric response over broadband may be more appropriate and allow for more robust and simplified signal acquisition schemes.

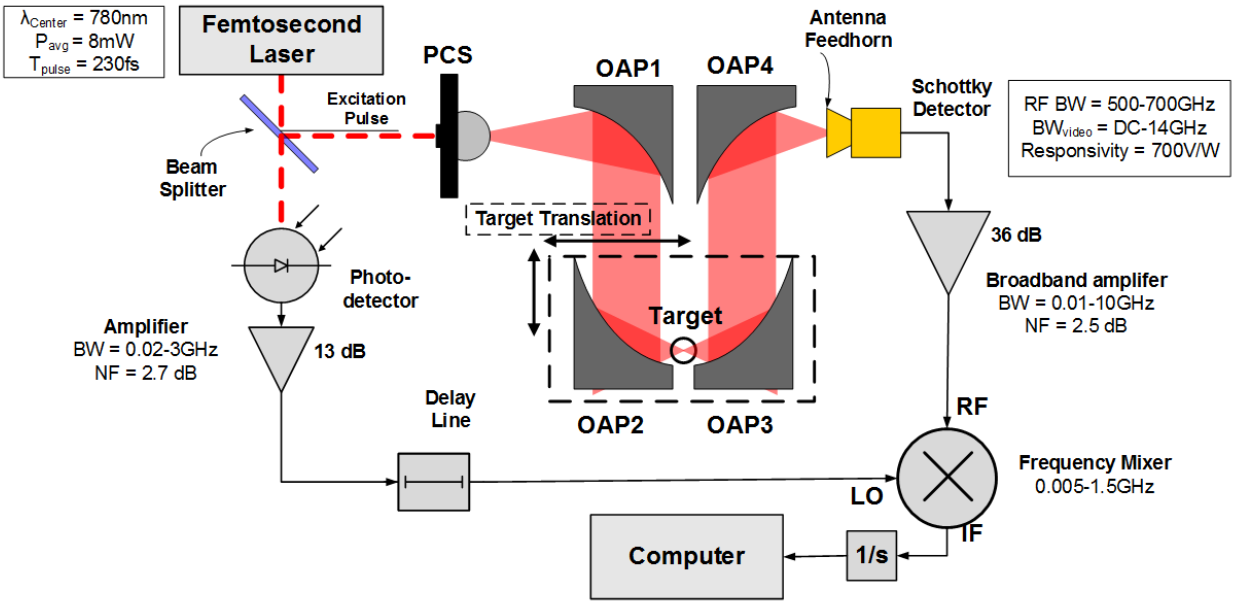


Figure 1-4. Block-diagram of a direct detection, reflective THz imaging system and components

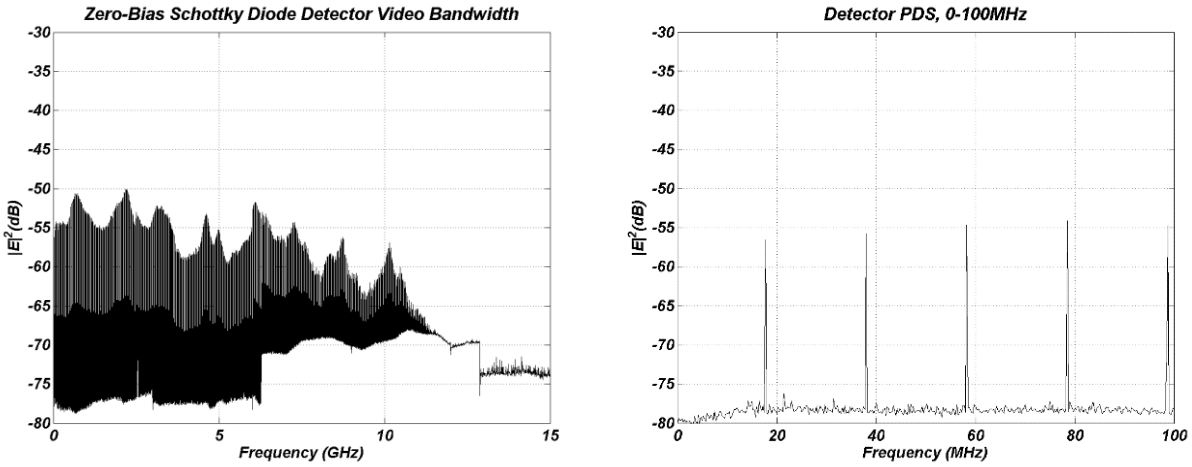


(a) (b)

Figure 1-5. Power Spectrum Density (PSD) of Zero-bias Schottky Diode detector showing video bandwidth (BW)

A direct-detection, reflective THz medical imaging system developed at the UCLA biophotonics laboratory is shown in Figure 1-4. A similar type of ultrafast laser (pulse duration: 230 fs, repetition rate: 20MHz) driven photoconductive switch is used as the pulsed THz source [14]. The THz pulse is collimated by a 1-inch clear aperture 90$^{o}$ off-axis parabolic mirror (OAP1) and focused to a target by another 90$^{o}$ off-axis parabolic mirror (OAP2). A pair of off-axis parabolic mirrors (OAP 2,3) serves as an "objective" set of mirrors to focus the incident THz beam to a target and collect the reflected beam centered at the specular direction. OAP3 outputs the re-collimated beam toward the final mirror with highest numerical aperture (OAP4) to focus the THz beam to the feedhorn of a zero-bias Schottky diode detector (Virginia Diodes, VA). The geometries and optical relay path is shown in Figure 1-6 and a photograph of the system is shown in Figure 1-7.

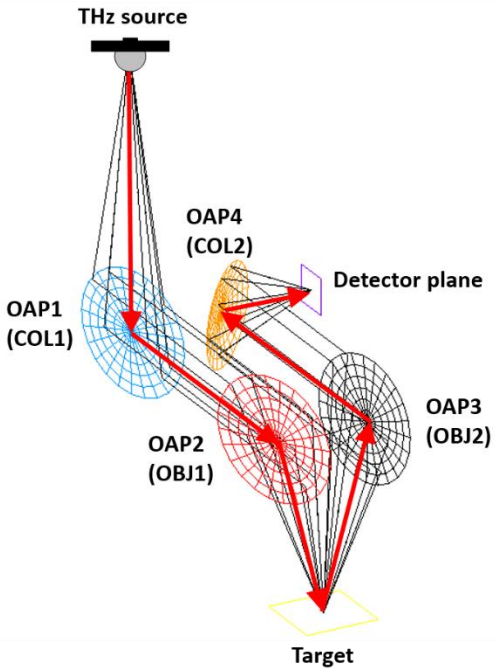


Figure 1-6. 90º OAP mirror components and THz beam relay path geometry of direct-detection reflective THz imaging system

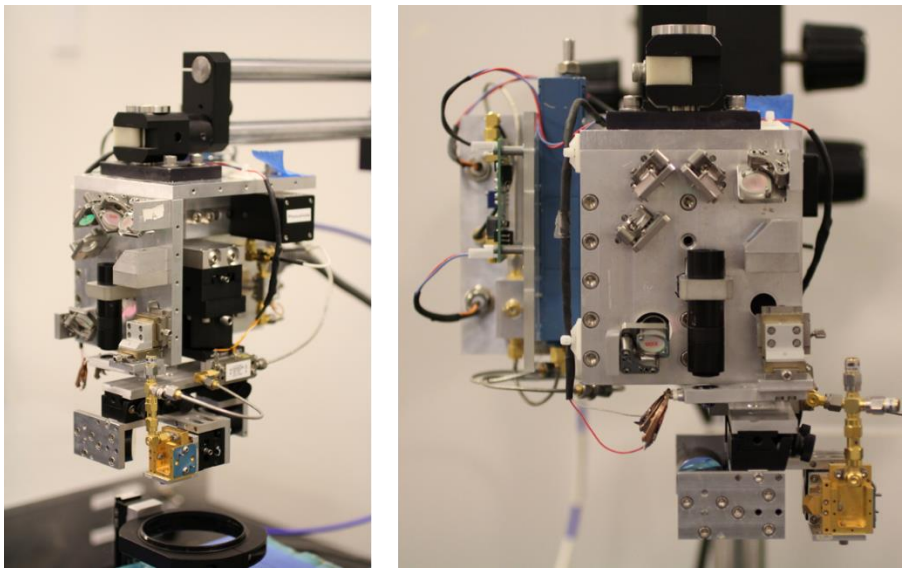

Figure 1-7. Direct-detection reflective THz imaging system at UCLA biophotonics laboratory

The fast response time of the zero-bias Schottky detector (ZBSD) allows rectification of THz pulse to baseband. The diode is mounted in WR 1.5 waveguide to select the detection band at 400-700GHz, and outputs rectified signal proportional to the electric field magnitude of the THz pulse. The detection signal to noise ratio (SNR) is determined by detector's video bandwidth, measured and plotted in Figure 1-5(a) (left). Resolved Power spectrum density (PSD) of detector output (Figure 1-5(b), right) confirms the 20MHz repetition rate of the driving femtosecond laser and the THz pulse rate. Following amplification by a broadband, low-noise amplifier (100MHz – 20 GHz), the rectified THz signal is further down-converted by the gated receiver scheme using a RF frequency mixer. The frequency mixer inputs THz signal at the RF port and the reference pulse as a gating pulse at the LO port. IF output is integrated and sampled at ADC to provide the pixel value. The signal value quantifies aggregate reflectivity of the target at the detection band (400GHz-700GHz). An Image is obtained by raster-scanning the target under the focal plane of the focusing objective mirrors (OAP2, OAP3). Direct detection design and construction shown in Figure 1-4 enables sufficient SNR and rapid pixel acquisition with mostly compact components, achieving 54dB of SNR per pixel with integration time of 3ms. The direct-detection system presented in this section is used as the example in the investigation of optical design considerations and measurement of THz scattering property in the subsequent sections.

# Chapter 2 Analysis of Quasi-optical Components in THz imaging

## 2.1. Optical Components in THz imaging

Free-space wavelength at 1 THz (l = 0.33mm) is approximately 1/75 of a 1 inch aperture. Considering the size of typical bench-top optical components and wavelength at THz region, geometrical optical techniques for analyzing propagation is a good approximation [17]. However, due to longer wavelength, diffraction analysis is relevant in many applications. Therefore, design and analysis of THz optical imaging systems using conventional optical elements is done with quasi-optical analysis.

Lenses in the THz region can be manufactured from plastic compounds such as High-density polyethylene (HDPE), polyethylene thermoplastics, Polymethylpentene compound (i.e. PMP or TPX$^{TM}$ – Mitsui, Japan) that is transparent in visible region, and Teflon. These are relatively cheap materials with tolerable effects of aberration and scattering from machine tool-marks by light polishing. [17] However, given the relatively weak output power of THz sources, systems employing lenses suffer from both Fresnel reflection losses and material attenuation.

For this reason, off-axis parabolic (OAP) mirrors are conventionally used in millimeter wave and THz regions. OAP mirrors are segments from one side of a full paraboloid, providing a focal point displaced from the mechanical axis. Parabolic mirrors are more efficient in light collecting (low loss), have high numerical aperture, and parabolic shape does not cause spherical aberration. Mirrors also do not introduce chromatic aberration. This property is especially relevant when the THz source is pulsed, such as that produced by an ultrashort pulse-driven photoconductive switch (PCS). However, OAP mirrors present drawbacks in sensitivity to alignment of optical axis and parallelism, and show strong coma if it is not illuminated exactly along its optical axis. In the design and development of a remote sensing and imaging system, efforts must be undertaken to

aid in understanding the effect of aberrations at the focal plane and polarization state when propagating electromagnetic waves through a series of mirrors. Usage of OAP mirrors in THz imaging design is not sufficiently discussed in the literatures, and therefore motivates this section.

## 2.2. Properties of 90° Off-Axis Parabolic (OAP) Mirror and Matched Pair of Objective Mirror Set Design

The direct detection THz system in Figure 1-4 employs four 90° OAP mirrors for THz relay design. THz illumination is focused and collected by the objective assembly based on matching pairs of OAP mirrors (Figure 2-2). The objective mirror pairs are configured such that the integrated assembly accepts and outputs parallel, collimated beams. The objective mirrors are rotated about its optical axis such that their clear-aperture normal vectors are parallel and their focal spots overlap, thus forming a conjugate pair. Each clear aperture of the objective is concentric with the clear aperture of the source and detector mirrors. Three different mirrors sets are designed with 1 inch, 2 inch, and 3 inch effective focal length (EFL) pairs of mirrors, and used to generate *in-vivo* THz images of burn wounds in [11, 14, 16]. Properties and performance characterization of each mirror sets are compiled in Table 2-1.

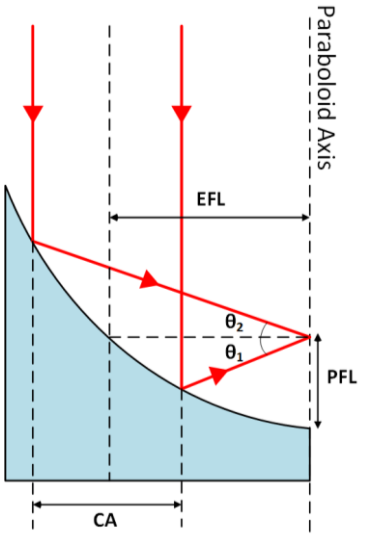


Figure 2-1. Numerical Aperture (NA) of 90° off-axis parabolic mirror

This design aims to facilitate simple adjustment of THz optics without perturbing the rest of the optical components alignment. Such a design is convenient for efficiently exploring tradeoffs between spot size, working distance, and incidence angle with different numerical apertures. However, the arbitrary rotation of the objective mirrors introduces aberrations of the imaging plane and polarization state, whose effects are not well understood.

Table 2-1 Properties of Matched Pairs of OAP Mirrors

| OAP EFL (mm) | $w_d$ (mm) | q (deg) | 10%-90% (mm) | DOF (mm) | $\theta_1$ (deg) | $\theta_2$ (deg) | $NA_{\theta 1}$ | $NA_{\theta 2}$ |
|---|---|---|---|---|---|---|---|---|
| 25.4 | 9.3 | 30 | 0.61 x 0.69 | 0.8 | 36.869 | 22.619 | 0.6 | 0.38 |
| 50.8 | 36.5 | 14 | 1.2 x 1.3 | 4.0 | 16.260 | 12.680 | 0.28 | 0.22 |
| 76.2 | 62.4 | 9 | 2.1 x 2.6 | 11.7 | 10.388 | 8.797 | 0.18 | 0.15 |

EFL = effective focal length
$w_d$ = working distance
q = Incidence angle
DOF = depth of field

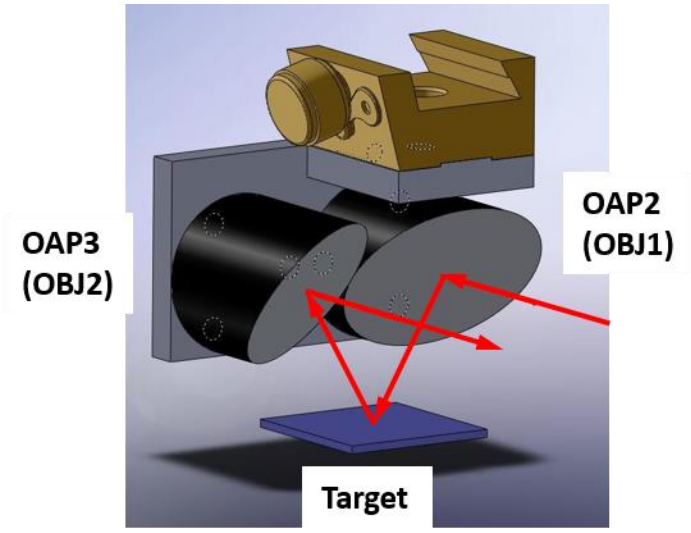


Figure 2-2. Objective OAP mirror set assembly showing central ray path

The spot size on the target is measured by the knife-edge method, in which a metal edge was swept in the imaging plane and the received power monitored as a function of edge displacement. This measurement yields the spatial step response of the system and can provide a good estimate of the point spread function with measurements performed in two orthogonal directions.

An objective mirror of higher numerical aperture additionally benefits from a smaller achieved focal spot at the cost of more sensitive alignment of the target to the focal plane (decreased DOF) and decreased working distance. In a general design consideration, the incidence angle is independent of mirror aperture though it would require re-positioning of the remaining optics. A more oblique incidence angle will afford better Fresnel reflection properties at the cost of a smeared focused spot and the effect of aberrations.

### 2.3. Analysis of Source Profile, Aperture, and OAP Focusing Properties

Geometrical propagation path of THz beam can be investigated with ray-tracing method, while more in-depth study of field distribution and polarization requires propagation of coherent wave (amplitude and phase) with polarization vector. The optical design of OAP mirror system in Figure 1-4 employing objective OAP mirror assembly sets is analyzed with Advanced Systems Analysis Program (ASAP) software platform (Breault Research, Tucson AZ).

#### 2.3.1. Source Profile

An appropriate model of the THz source profile is constructed. Directly measuring the radiation profile from the Silicon hyper-hemispherical lens-coupled PCS is challenging, as the sensitive optical alignment of the Auston switch (PCS) and free-space 780nm femtosecond laser restricts any mechanical translation of the source device. Furthermore, due to relatively low THz power

output, signal observed by THz detectors suffers from low SNR, making it difficult to use conventional antenna beam pattern measurement techniques.

Instead, the source device used in the system is viewed as a lens-coupled antenna system with circular aperture, whose output can be approximated as Gaussian [17]. With Gaussian beam profile, scalar-diffraction theory can be used to predict radiation patterns of apertures with non-uniform illumination. Beam profile from circular aperture with Gaussian illumination distribution, in the lateral plane with respect to the axis of symmetry, results in a radiation pattern that is also Gaussian in the far-field [23]. Furthermore, even for extreme values of $a/\lambda$ (a = aperture diameter), most of the energy is contained in the main lobe. Hence, in the following analysis, the THz source beam pattern is assumed as a circularly polarized, $TEM_{00}$ mode Gaussian beam with $10^o$ divergence angle [24], and diffraction-limited beam waist position at planar antenna. At far-field, the source profile can be equivalently written as a single Gaussian beam with a beam waist at the planar antenna location and the waist radius $w_o$ given by

$$\theta = \frac{\lambda}{\pi\omega} \qquad (2)$$

Using (2), a $TEM_{00}$ mode linearly polarized (x and y each) Gaussian beam source is created to have the beam radius of 0.91mm and $10^o$ divergence angle. The beam waist position is aligned at the focal point of the OAP1. The cross-section of the Gaussian beam profile and polarization is shown in Figure 2-9a.

2.3.2. Effect of Mirror Configuration in Imaging Plane Distortion

System optical components and their geometries are constructed in ASAP platform. An OAP mirror is defined by cutting out a portion of a paraboloid, with a 1" clear aperture, variable EFL (by changing the radius of curvature of the mirror), and assigned 100% reflectivity at the mirror

surface. The THz objective mirror set design described in the aforementioned section is also implemented by conjugate rotations of each mirror (-θ and θ) about its optical axis.

Optical design and relaying of the THz beam are tested with geometrical propagation (ray-tracing) methods. As expected, the focusing properties of parabolic mirrors are ideal as long as the input beam is perfectly collimated. Precise positioning of point-source at the focal point of the first mirror (OAP1) produces perfect alignment of all rays to the detector location.

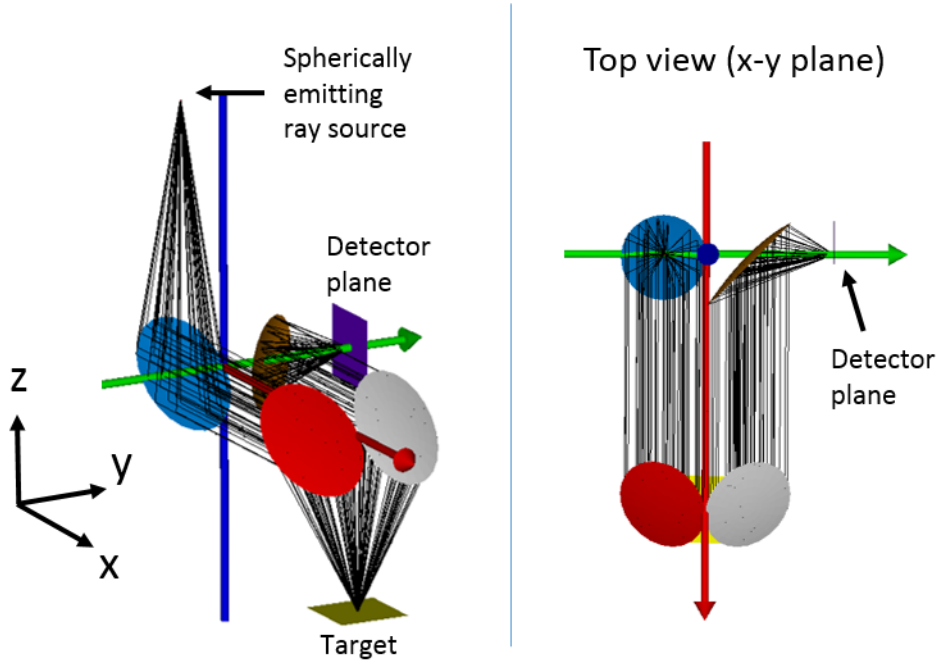


Figure 2-3. Ray tracing analysis of optical component geometry in the direct-detection THz imaging system

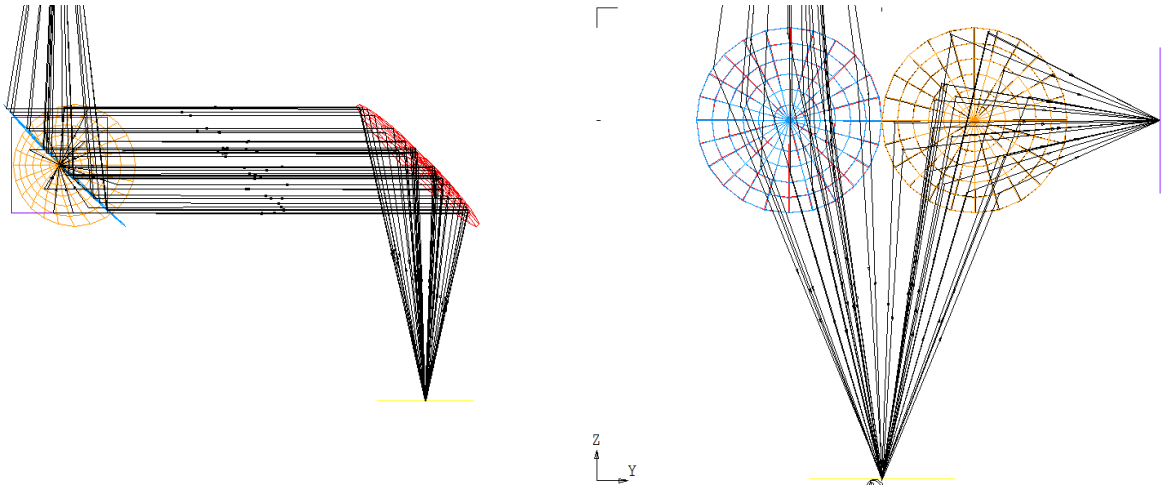


Figure 2-4. Ideal arrangement of THz point-source, OAP mirrors, and detector plane to achieve geometrically ideal focusing

The first source of deviation from ideal behavior is the finite source dimension. A perfect point source placed at the focal point of the collimating mirror produces a perfectly collimated beam, and a perfectly focused spot at the target in geometric ray tracing, confirming the property of OAP mirrors. As the source aperture size becomes reasonably larger than the wavelength, aberrations at the focal point are observed.

An investigation of tilting of imaging plane reported by [25] is performed with different mirror configurations – PARA and ORTHO – on the focal spot at the target. With the calculated beam waist (0.91mm) less than twice the wavelength (0.5mm), ray tracing analysis shows minimal aberration of the focal point at the target comparable to Figure 2-4. Keeping the PARA configuration, the source aperture diameter is increased to $a/\lambda = 5$, 10, and 20 in circular aperture cross sections, uniformly illuminated, and centered at the axial focal point of COL1 (Figure 1-4). Increasing the aperture size produces more severe aberrations at the focal point in the PARA configuration, shown in Figure 2-6. It is observed that rather than 'tilting' of the plane, the aberration appears to resemble that of spherical aberration produced in spherical mirrors.

By contrast, in ORTHO configuration the aberration at the focal point vanishes and almost perfect geometric focusing is observed with an aperture size of $a/\lambda = 20$. Ray plots in Figure 2-6 are taken at the same window. In both cases, converging point of the rays occur above the actual focal point as the source dimension is increased. Matched ORTHO orientations are desired in the system that employs multiple sets of mirrors to relay any optical beam.

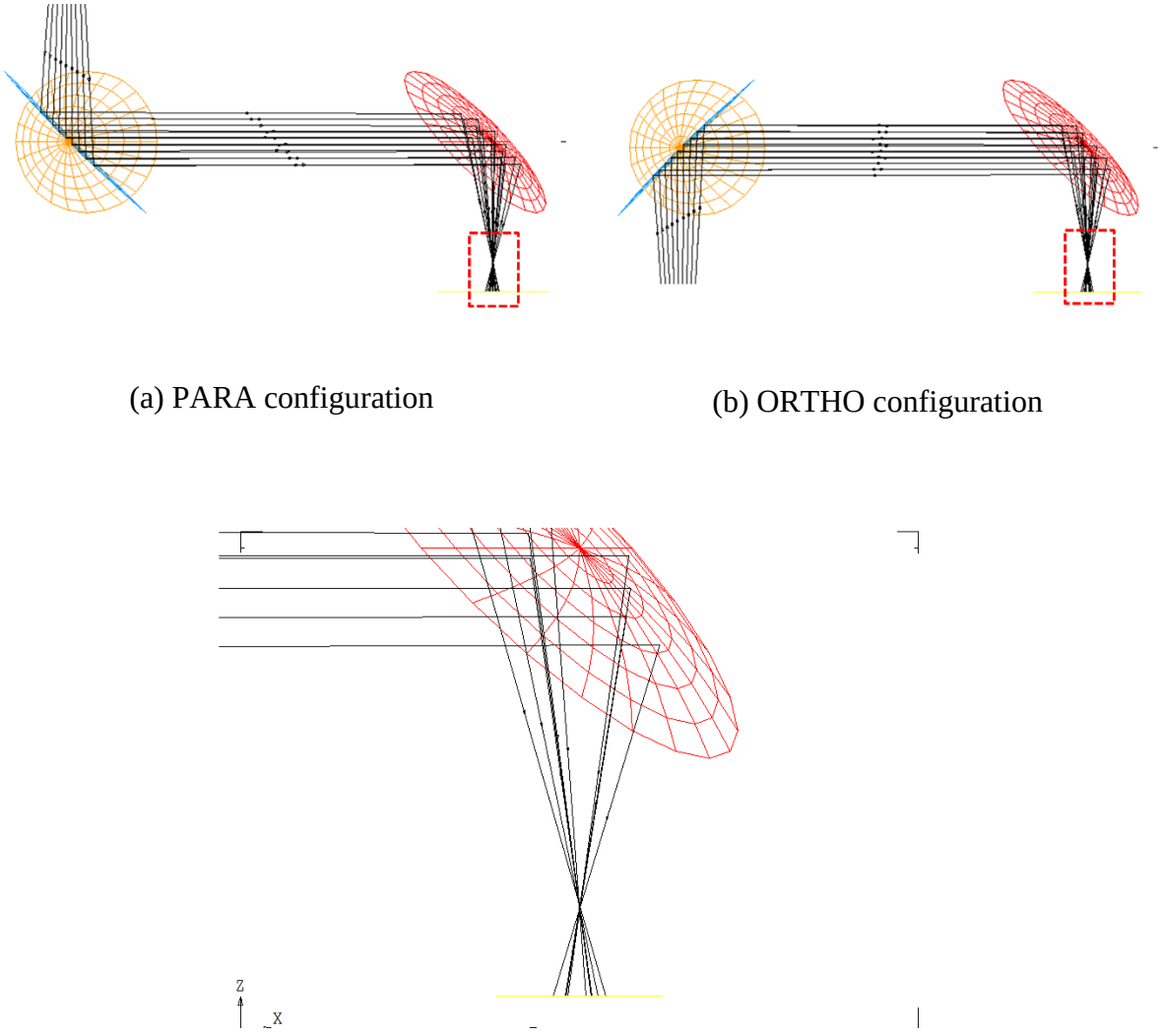


(a) PARA configuration

(b) ORTHO configuration

(c) Zoomed-in region near the focal point

Figure 2-5. PARA and ORTHO mirror orientation

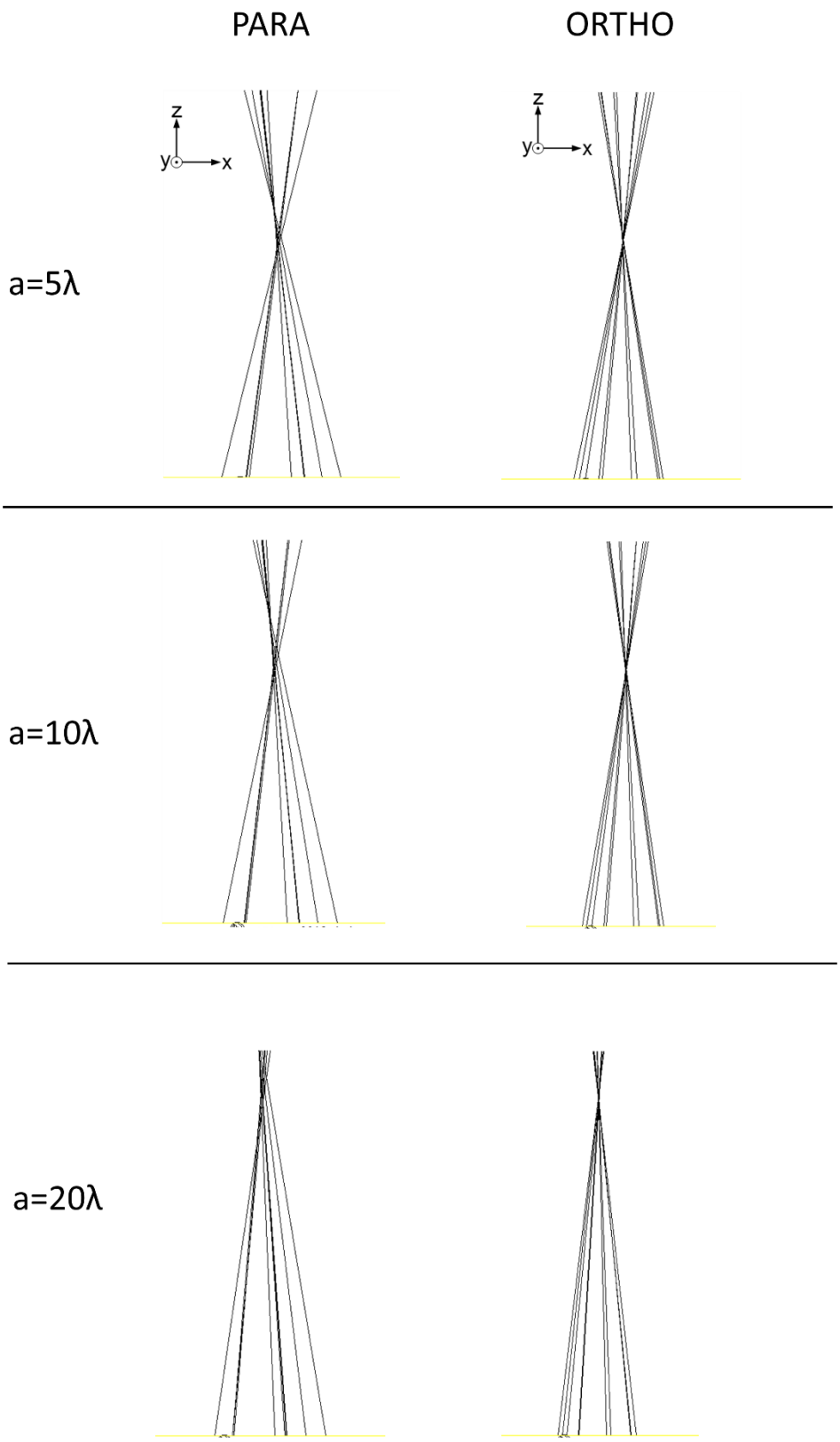


Figure 2-6. Focal point formation in PARA and ORTHO mirror orientations

## 2.4. Propagation of Gaussian Beam through a Series of OAP Mirrors

### 2.4.1. Simulation Design

Gaussian beam propagation methodology employed by ASAP platform allows propagation of wave vector field with arbitrary source profile through a series of optical components [26]. Spatially resolved field energy distribution (beam pattern) and polarization state profile of the beam are sampled at each key routes of propagation. The simulation is performed at λ=0.5mm (0.6 THz) to observe the effect of coherent diffraction. Figure 2-7 shows an overview of beam propagation through THz optical components. At each point of analysis, the THz beam is intercepted at a plane orthogonal to the optical axis of the mirror. The beam profile and polarization are computed and displayed.

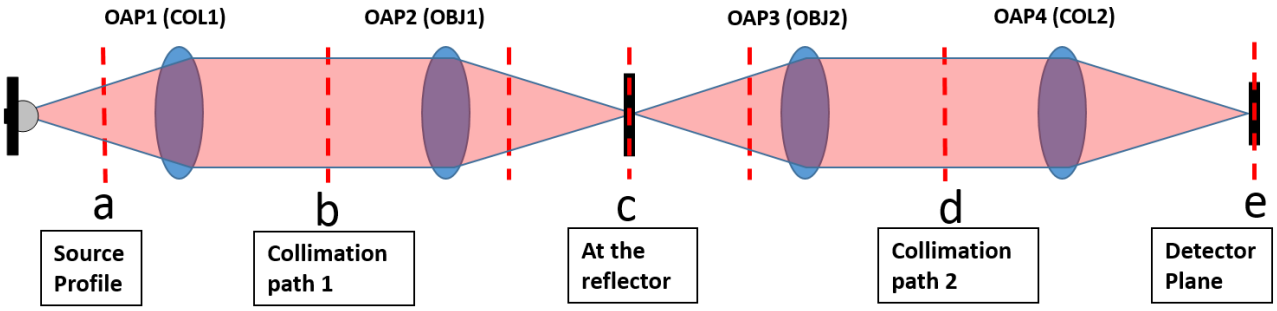


Figure 2-7. Overview of analysis of THz beam propagation through a series of OAPs and a reflector target

Figure 2-9 a through e are generated from the sampling of field energy and polarization state of the cross-sectional of the beam, (marked as dotted red lines in Figure 2-7. Overview of analysis of THz beam propagation through a series of OAPs and a reflector target (Figure 2-7) for a x-polarized source and 2-inch objective EFL mirror set (OBJ 1 and 2). The source profile is confirmed in Figure 2-10a, having uniform linear polarization and Gaussian beam profile. The source underfills the aperture of the first collimating mirror (COL1), producing a beam diameter of ~17mm. The profile of the collimated beam (Figure 2-9b) shows expected collimation of beam.

Effects of polarization aberration from the first reflection are observed at locations away from the Y-axis of the reflection, however at the Y axis the polarization state is preserved. Simulation is continued with separate propagation of orthogonal polarization components from this point forward. Re-sampling of beam profile before and after the reflection from the target (reflector) was necessary for the stability of the simulation. Asymmetric distribution of the first diffraction lobe is observed due to the rotation of the mirror (figure not shown). This effect is discussed in the following section with comparisons to different rotation angles.

The focused spot on the reflector target is shown in Figure 2-8. The main lobe's diameter of 1.6mm, close to the 1/λ diffraction limited spot size. The observed spot diameter agrees with that computed by [24] using ray-transfer matrix with Gaussian beam parameters q and p. It is observed that the polarization at the spot is slightly rotated as (Figure 2-9c). Presence of cross polarization components produces circular polarization states at the higher-order lobes due to path length difference.

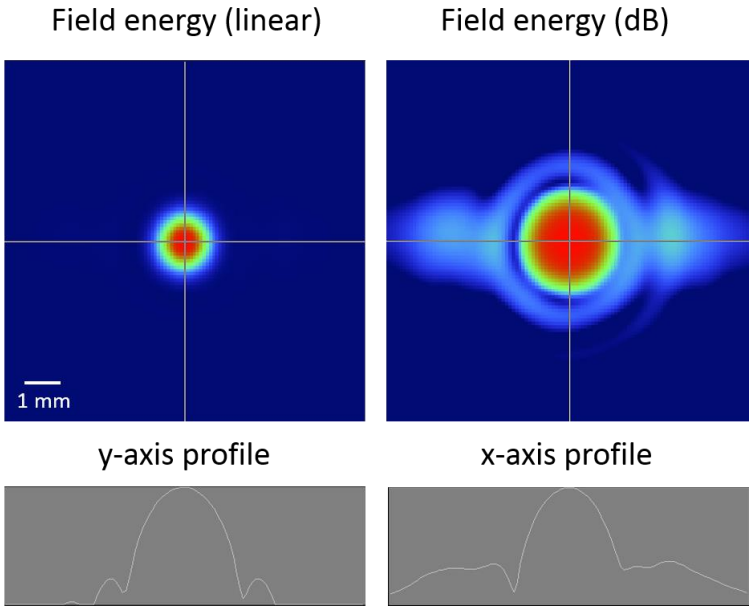


Figure 2-8. Field energy plot at the focal spot of 2" EFL objective assembly at 600GHz

The beam profile at ‘collimation path 2’ shows a pronounced effect of asymmetry of beam intensity distribution, in contrast to the first collimated path (Figure 2-9 b and d). The centroid point of the beam is computed to be well over 2000mm away from the beam position, indicating that the beam is still well collimated and the beam diameter remains close to the size of the clear aperture. Polarization rotation is also highly asymmetric due to the rotation of the objective mirror. The collimated beam is collected by the next OAP mirror (COL2) with focal length of I inch, and focused to a detector plane. The focused spot has a diameter of 0.7mm, also near the diffraction limit, and agrees well with that calculated by ray matrix transfer method. [24] At the focused main lobe, rotation of the polarization is most pronounced. Path length difference of the cross-polarization component is observed as circular polarization state at the side lobes of the beam.

Similar analysis is performed with a y-polarized incident beam. The source profile and the polarization state is confirmed in Figure 2-10. Although the polarization axis and the mirror axis orientation are orthogonal to the previous case, similar polarization aberration effects are observed in Figure 2-10 b through e. The degree of polarization aberration appears to be similar throughout the various folds of the mirrors. The polarization cross sections of x-polarized and y-polarized cases almost match at respective points, if the polarization plots are rotated 90 degrees. The final polarization state at the detector plane appears to be similar to that in Figure 2-9-e. The cross-polarization component is most developed at this stage, and circular polarization state is observed at the higher order lobes.

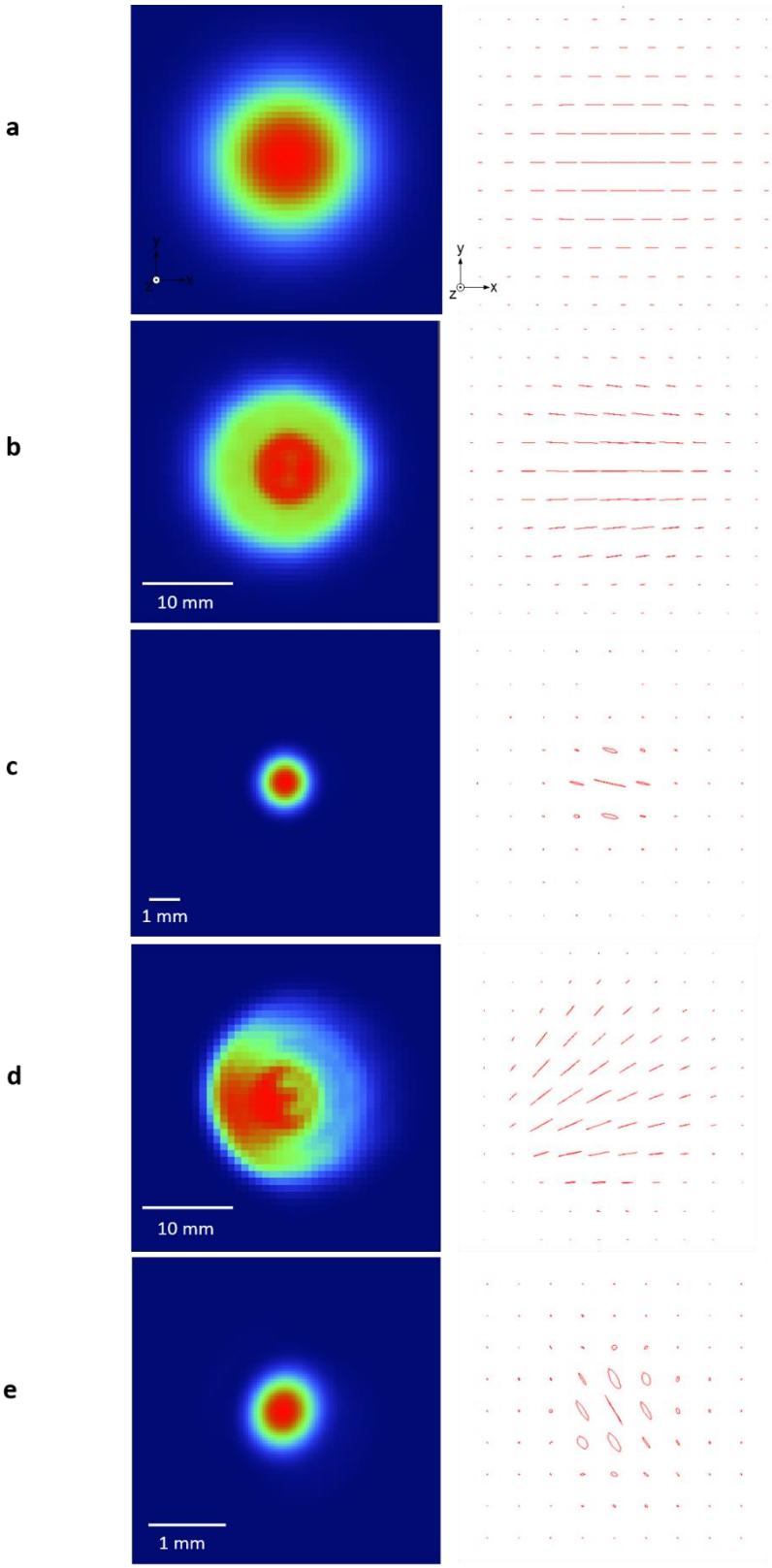


Figure 2-9 THz beam profile and polarization state while propagating through a series of OAP mirrors, from an x-polarized Gaussian $TEM_{00}$ source.

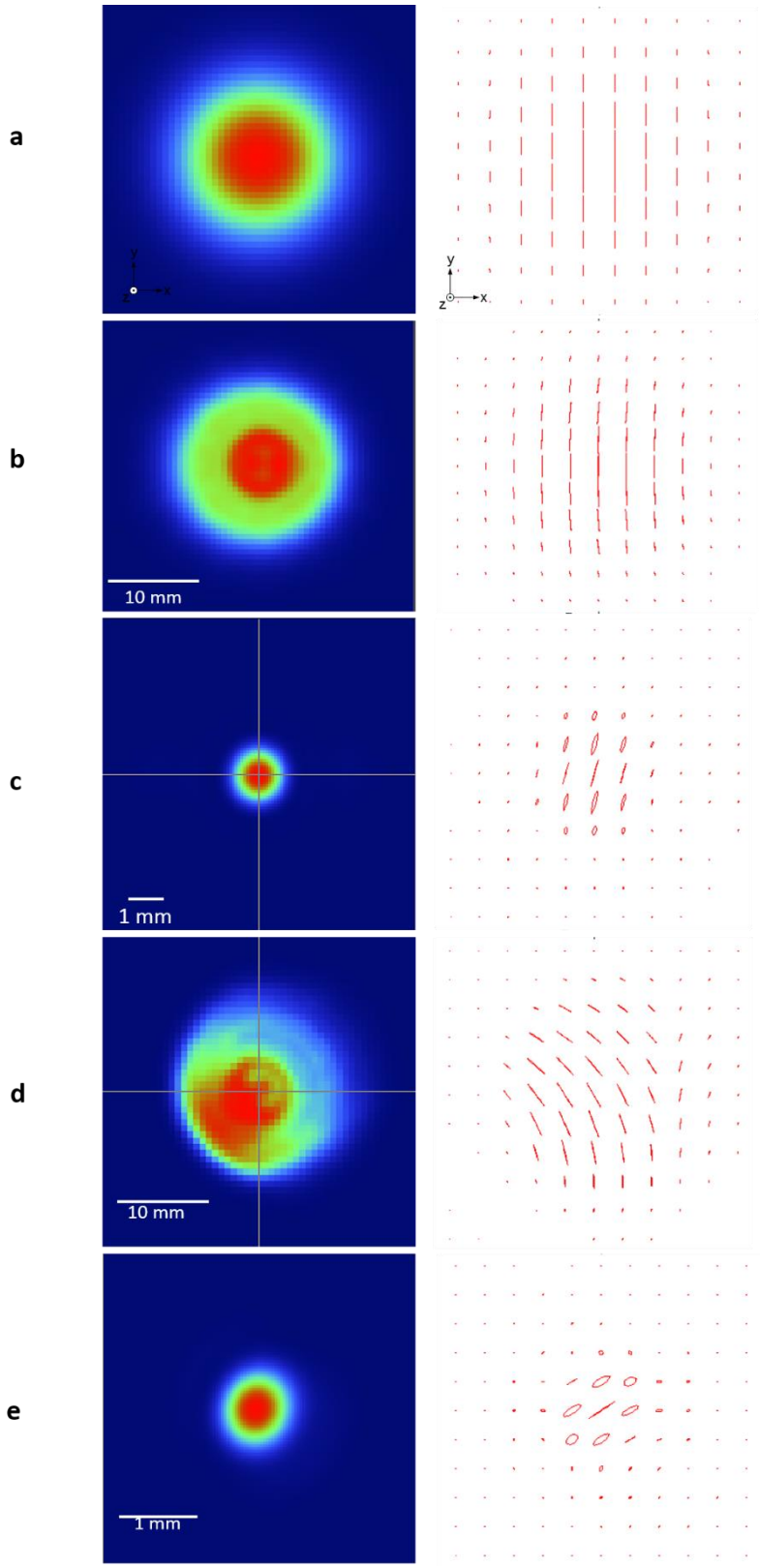


Figure 2-10 THz beam profile and polarization state while propagating through a series of OAP mirrors, from a y-polarized Gaussian $TEM_{00}$ source.

2.4.2. Comparison with Different Numerical Aperture Objectives

The objective mirror set is replaced with a smaller or larger numerical apertures. While rotations of the objective mirrors are independent of the numerical aperture consideration, the current design of the mirror sets allows to observe impact of different incidence angles by mirror's focal points, as shown in Table 2-1. The 2-inch objective mirror sets are replaced with a 3-inch set, and the reflector plane is re-positioned at the focal point of the objectives. Figure 2-11a-c compiles the computed field energy distributions in linear and dB scale, and the polarization state in the same window; plots a,b,c are generated at the focal point (at the reflector), collimation path 2, and at the detector, respectively.

Smaller numerical apertures with longer Rayleigh length produce larger spot sizes as predicted (Figure 2-11a, page 27). The smaller incidence angle ($9^o$) produces a more symmetric intensity distribution compared to the Figure 2-8, in which the incidence angle was $14.5^o$. The rotation of the polarization angle at the focal spot is also observed, however to a lesser degree due to the smaller incidence angle. Asymmetric distribution is still observed at the collimation path, however the field energy cross-section in log scale shows the best collimation property among all mirror sets. The focused spot at the detector plane (Figure 2-11c) shows a cross polarization component and resulting circular polarization state.

In comparison, larger incidence angle and sharper focus by the 1-inch mirror set produce the most cross polarization components and asymmetric distribution of beam profile. Field energy distribution in linear and log scale and the polarization state are shown in Figure 2-12a-c, at the focal spot in the target, collimation path 2, and at the detector plane, respectively. A spot size of 0.7 mm is achieved, agreeing with that measured in Table 2-1 with an appropriate input Gaussian

beam parameters and the focal distance of the mirror [24]. Most noticeable differences are present in the highly asymmetric distribution in the cross-section of the collimated beam (
Figure 2-12b) and visible rotation of the spot shape, direction and polarization state at the detector plane (Figure 2-12c). Changes in the shape of the focal spot from the 1-inch mirror set suggests angular alignment of detector orientation may be considered for more efficient coupling.

### 2.4.3. Summary

THz optical design in the UCLA's imaging system is studied as an example of relaying THz beams using $90^o$ off-axis parabolic (OAP) mirrors. As it is demonstrated in [25], compensating mirror configuration is desired to avoid distortion and tilting of imaging plane. However, as long as the source profile aperture is maintained below five wavelengths, such effects are tolerable.

Characterization of the focused aperture of the objective mirrors agree well with optical simulation using a $TEM_{00}$ Gaussian beam source model. A Gaussian source beam profile minimizes the effect of diffraction lobes and produces "well behaved" beam parameters after multiple interactions with optical components. Using a linearly polarized Gaussian beam source profile, propagation of cross-polarization components are investigated in a $90^o$ OAP mirror system. While propagation of finite cross section beams through a series of fold mirrors inevitably introduces polarization aberration, it is observed that the rotation of the mirror axis appears to enhance cross-polarization components.

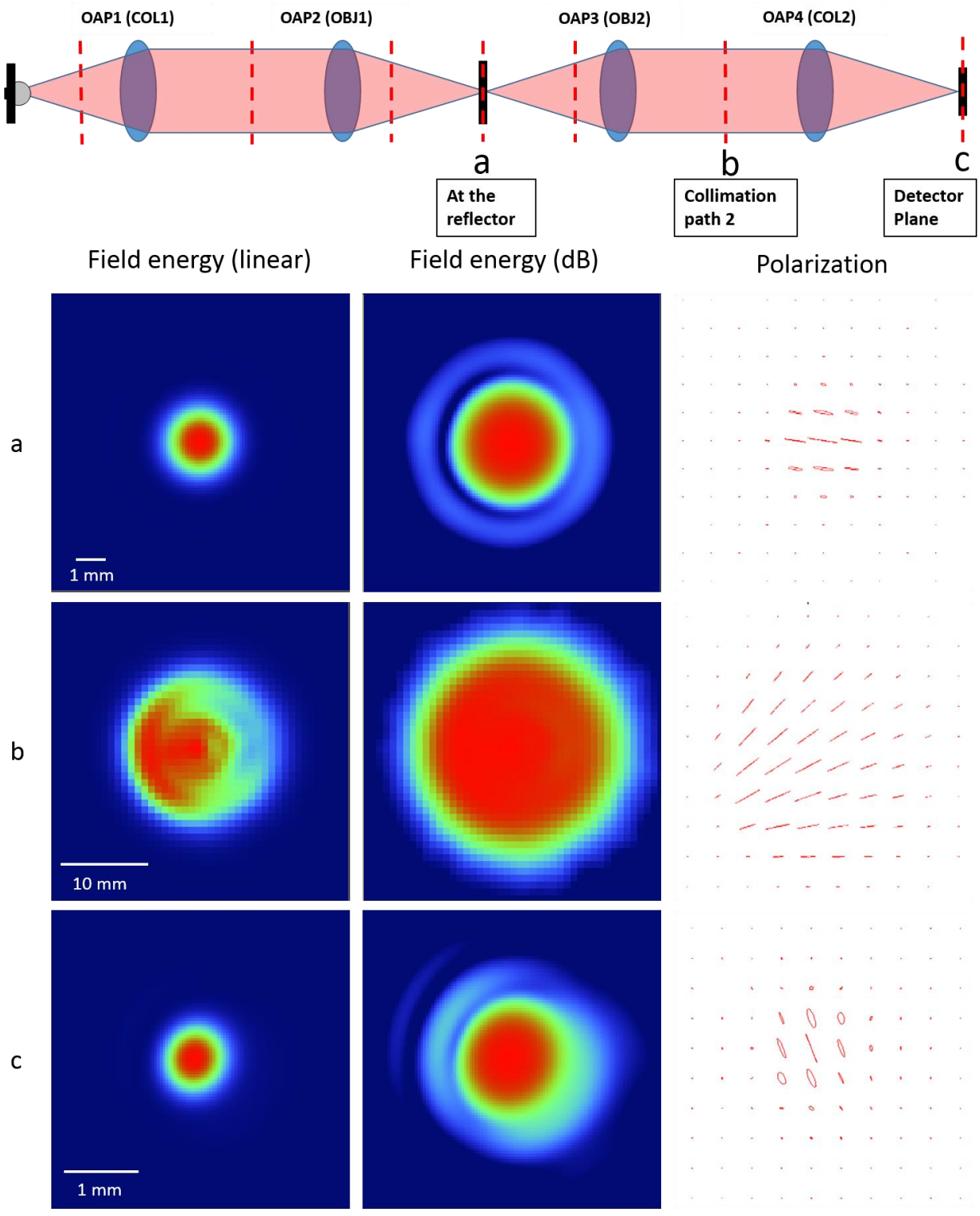


Figure 2-11 THz beam profile and polarization state in 3-inch objective mirror system

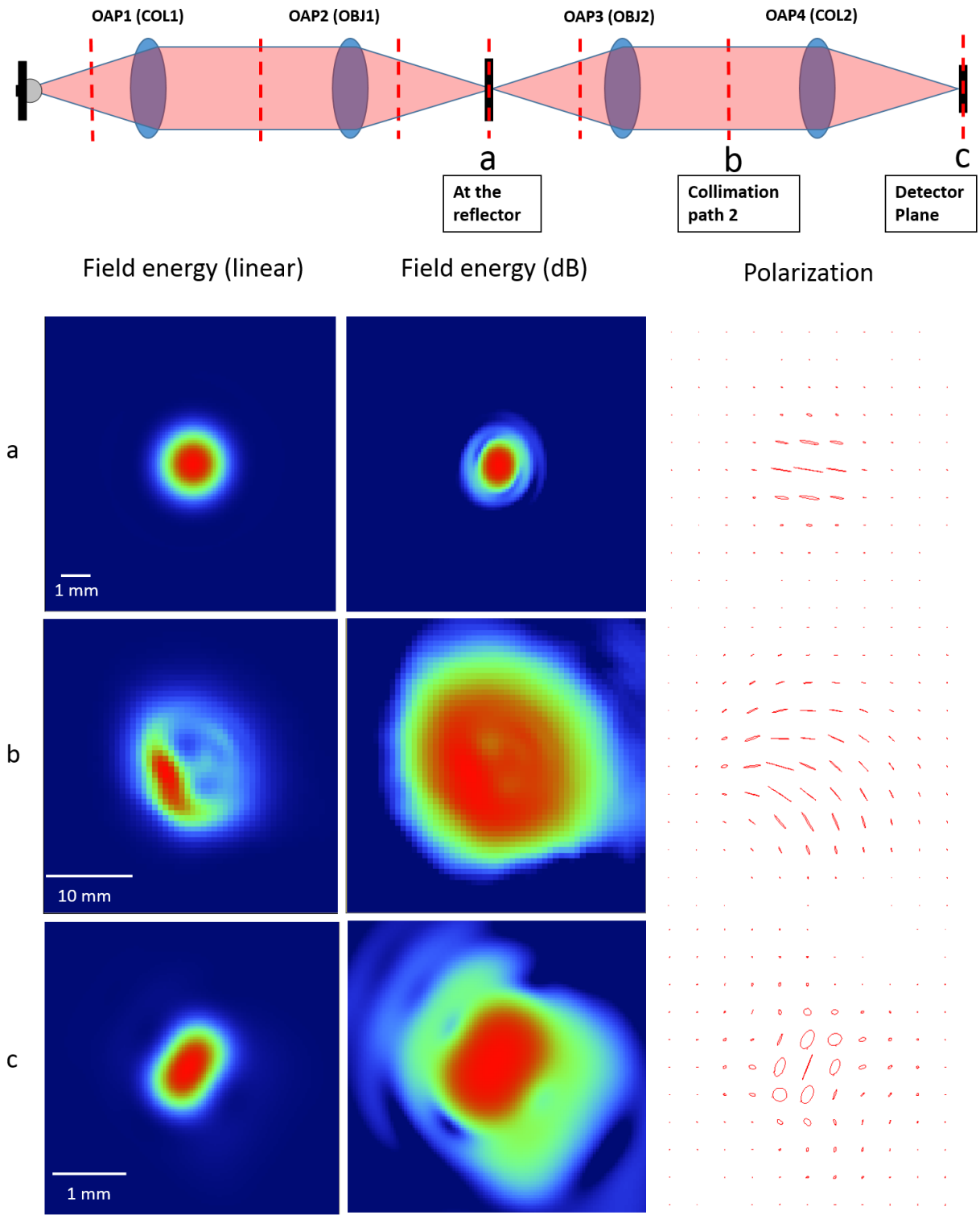


Figure 2-12 THz beam profile and polarization state in 1’’-inch objective mirror system

# Chapter 3 Rough surface scattering in THz imaging

In reflection mode THz imaging, irregularities of the surface interface scatters electromagnetic waves to random direction, and confounds the interpretation of collected scattered field as signal. Therefore it is necessary to understand the how, and how much the surface roughness will contribute to the uncertainties in collected signal, and properly characterizing bulk/surface scattering of light in physiological tissue are crucial in realizing medical sensing devices.

Scattering from a rough surface is typically analyzed as a function of wavelength of the incident wave, as well as by the intrinsic properties of the material at the interface. A definition of 'rough' depends much on the nature of the problem, the method of analysis, and intended applications. Depending on what is useful, the definition of the "rough" have to be somewhat arbitrary. A loose criteria that generally defines "smooth" surface is the Rayleigh criterion, considering the surface is "smooth" if the phase difference between the two parallel rays, scattered to the specular direction from the non-uniform surface, is within $\pi/4$, or $h < \lambda/8\sin\gamma$, where $\lambda$ is wavelength, $\gamma$ is incidence angle, and h is height difference between two point. A more strict criterion, Frauenhofer criterion states phase difference be less than $\pi/8$, or $h < \lambda/32\sin\gamma$ [27].

A more rigorous view of the scattering from rough surface is diffuse direction of scattering according to how rough the surface is. While closed form solutions are sometimes possible for rough surfaces with periodic features, such as those for scattering from gratings and lattices, analysis for irregular rough surfaces requires statistical descriptions of the surface and stochastic (random process) description of scattered wave.

3.1. Scatter Theory: General Kirchhoff Solution for Scattering

Kirchhoff Approximation (KA) theory allows to combine statistical description of the rough surface and prediction of scattered field distribution. Application of KA can be extended to THz region because of its general approach to express the scattered field in terms of ratio between wavelength and roughness feature dimension. Kirchhoff Approximation/ scattering theory is based on the formulation of continuous 1 or 2-dimensional surface and the integral equation of scattered wave using physical optics principle. KA originally appears in the analysis of scattering of acoustic waves from the rough surfaces (sea surface, land, etc) [28]. In order to understand basis of theoretical approach and applicability of this scattering theory in the THz region, key details of approach by [29] is re-traced in this section with some modification.

3.1.1. Scattered Field

Kirchhoff approximation uses Kirchhoff-Helmholtz (KH) integral to write exact solution to scattering of plane wave from a 1-D surface with boundary conditions.

$$E_{scatter} = \frac{1}{4\pi} \iint_S \left( E \frac{\partial \psi}{\partial n} - \psi \frac{\partial E}{\partial n} \right) dS \qquad (3)$$

where

$$\psi = \frac{e^{jk_2 R'}}{R'}$$

is free-space Green's function, and scattered field wave number $k_2$ is determined by the boundary condition. KH integral equation allows to calculate the field induced by sources scattered by finite boundaries if we know the scattering surface geometry. The 1-D surface is defined to be $\zeta(x)$, extending from –L to L.

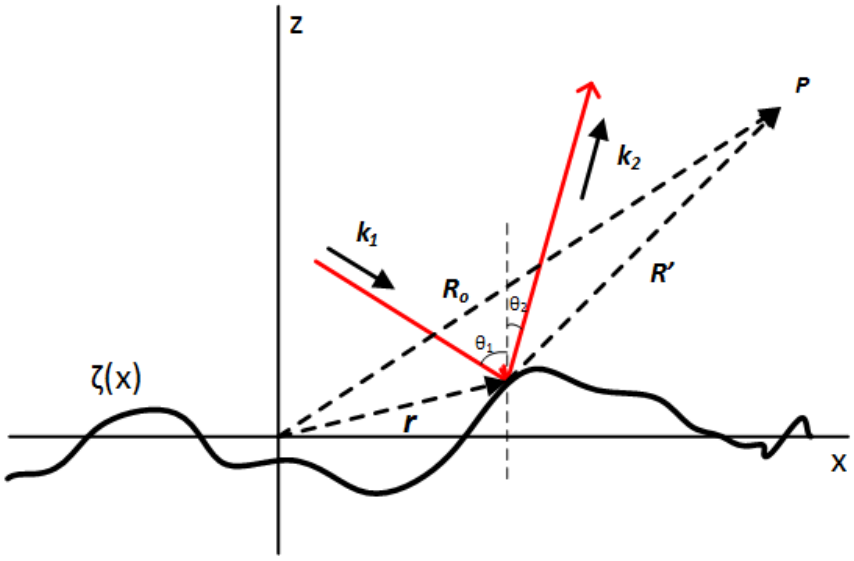


Figure 3-1. Scattering of a planar wave at a rough surface

Using the assignment of parameters shown in Figure 3-1, equation (3) is written in the following form at far-field [29]:

$$E_2 = \frac{jke^{jkR_o}1}{4\pi R_o}\int_{-L}^{L}(a\zeta' - b)e^{i(v_x x + v_z \zeta(x))}dx$$
$$a = (1-R)\sin\theta_1 + (1+R)\sin\theta_2$$
$$b = (1+R)\cos\theta_2 - (1-R)\cos\theta_2 \qquad (4)$$

Where

$$\boldsymbol{v = k1 - k2}$$

$$\boldsymbol{v} = \mathrm{k}(\sin\theta_1 - \sin\theta_2)\mathbf{x_o} - \mathrm{k}(\cos\theta_1 + \cos\theta_2)\mathbf{y_o}$$

$$\mathrm{v_{xy}} = \sqrt{\mathrm{v_x} + \mathrm{v_y}}$$

$\theta_1$ – incident angle
$\theta_2$ – observing angle
***k1*** – incident wave wavevector
***k2*** – scattered wave wavevector
R – Reflection coefficient from Fresnel Equation.

Defining $\rho = E_2/E_{2o}$ to be the normalized scattered field, where $E_{2o}$ is the field strength reflected from a perfectly flat surface, above can be written as:

$$\rho = \frac{1}{4L\cos\theta_1}\int_{-L}^{L}(a\zeta' - b)e^{j(v_x x + v_z \zeta(x))}dx \quad (5)$$

For a perfectly smooth surface with $\zeta(x) = 0$, the above integral gives $\rho=\text{sinc}(v_xL)$, the expected scatter pattern of a conducting finite sheet or an aperture. Equation (5) can be evaluated with appropriate value of **a** and **b**. For the simplicity of analysis, when the reflectance is independent of x (perfectly conducting surface), the reflection coefficient becomes unity and the coefficient **a** and **b** becomes constant. Equation (5) is simplified to:

$$\rho = \frac{F_2}{2L}\int_{-L}^{L} e^{j(\vec{v_x}\bullet\vec{r})}dx \quad (6)$$

Where

$$F_2 = \frac{1+\cos(\theta_1+\theta_2)}{\cos(\theta_1)+\cos(\theta_2)} \quad (7)$$

For a perfectly conducting surface, a similar result can be obtained for the magnitude (hence not considering polarization component) of scattered wave from 2-dimensional surface as equation (8). At specular direction, both $F_2$ and $F_3$ becomes unity.

$$\rho = \frac{F_3}{A_1}\iint_{A} e^{j(\vec{v}\bullet\vec{r})}dxdy \quad (8)$$

with

$$F_3 = \frac{1+\cos(\theta_1)\cos(\theta_2)-\sin(\theta_1)\sin(\theta_2)\cos(\theta_3)}{\cos(\theta_1)(\cos(\theta_1)+\cos(\theta_2))} \quad (9)$$

3.1.2. Treatment of Random Rough Surface

Equation (6) or (8) may be numerically evaluated for a specific, defined surface $\zeta(x,y)$. For a random surface, the surface profile $\zeta(x,y)$is expressed in a statistical description of roughness. The

general expression of expected mean and the variance at an observing angle can be found in terms of first-moment-generating function of the random surface.

If $\zeta(x)$ is a random variable assuming values z with a probability density w(z) and $<\zeta(x)> = 0$, the expected value of the integral from (6) can be written as follow.

$$\left\langle \int_{-L}^{L} e^{j(\vec{v_x}\bullet\vec{r})} dx \right\rangle = \int_{-L}^{L} e^{j(\vec{v_x}x)} \left\langle e^{jv_z\zeta} \right\rangle dx = \left\langle e^{jv_z\zeta} \right\rangle \int_{-L}^{L} e^{j(\vec{v_x}x)} dx \qquad (10)$$

Defining the moment-generating function $\chi(v_z)$

$$\chi(v_z) = \left\langle e^{jv_z\zeta} \right\rangle = \int_{-\infty}^{\infty} w(z) e^{jv_z z} dz \qquad (11)$$

equation (10) can be written in terms of $\chi(v_z)$

$$\left\langle \int_{-L}^{L} e^{j(\vec{v_x}\bullet\vec{r})} dx \right\rangle = \chi(v_z) \int_{-L}^{L} e^{j(\vec{v_x}x)} dx \qquad (12)$$

Where w(z) is the distribution of the height profile $\zeta(x)$. The expected mean of the normalized scattered field ρ is therefore:

$$<\rho> = \chi(v_z) \int_{-L}^{L} e^{jv_x x} dx = \chi(v_z)\,\mathrm{sinc}(v_x L) = \chi(v_z)\rho_o \qquad (13)$$

The variance D(ρ) is

$$D\{\rho\} = <\rho\rho^*> - \langle\rho\rangle\langle\rho^*\rangle \qquad (14)$$

Where $<\rho\rho^*>$ can be written from (6), to be

$$<\rho\rho^*> = \frac{F^2}{4L^2} \iint_A e^{jv_x(x_1 - x_2)} < e^{jv_z(\zeta(x_1) - \zeta(x_2))} > d\,x_1\, d\,x_2 \qquad (15)$$

3.1.3. Normally Distributed Surface

A profile of rough surface has a randomly distributed height. The statistical distribution of their deviation from a certain mean level can describe how "rough" surface is. When the surface height

distribution is a Gaussian, standard deviation σ characterizes such parameter. On the other hand, a random surface ζ(x) will have the autocorrelation function that describes how the adjacent surface profile is correlated, or how "irregular" is the surface. While the first definition is mostly reported in the roughness measurement, the latter definition, which can be regarded as "roughness spectrum" is equally important description of the roughness.

Normally distributed surface is taken as the most important and typical of naturally occurring rough surface. Such surface has surface height distribution of

$$w(z) = \frac{1}{\sigma\sqrt{2\pi}} e^{-z^2/2\sigma^2} \qquad (16)$$

whose moment generating function is

$$\chi(z) = \exp\left(-\frac{1}{2\sigma^2 v_z^{\,2}}\right) \qquad (17)$$

Substituting (17) into (13), the expected (mean) signal strength can be found:

$$<\rho>=\rho_o \exp\left[-\frac{2\pi^2\sigma^2}{\lambda^2}(\cos\theta_1+\cos\theta_2)^2\right] \qquad (18)$$

At the specular direction ($\theta_1=\theta_2$),

$$<\rho>_{spec} = \exp\left[-\frac{1}{2}\left(\frac{4\pi\sigma\cos\theta_1}{\lambda}\right)^2\right] \qquad (19)$$

Where the exponent term in (19) can be parameterized as

$$g = \left(2\pi\frac{\sigma}{\lambda}(\cos\theta_1+\cos\theta_2)\right)^2 \qquad (20)$$

The above expression is called the Rayleigh roughness factor [30] to express the decay in the specular direction mean signal due to rough surface scattering. The expected value ρ of amplitude at specular direction, normalized to the amplitude of the incident wave gives the Rayleigh

roughness factor in the modified Fresnel reflection coefficient. This result predicts decreasing signal strength due to diffuse scattering at rough surface as the frequency increases (or g number becomes larger) and the height profile of the roughness increases. Figure 3-2 plots ρ corresponding to the normal height deviation σ=30μm to 150μm.

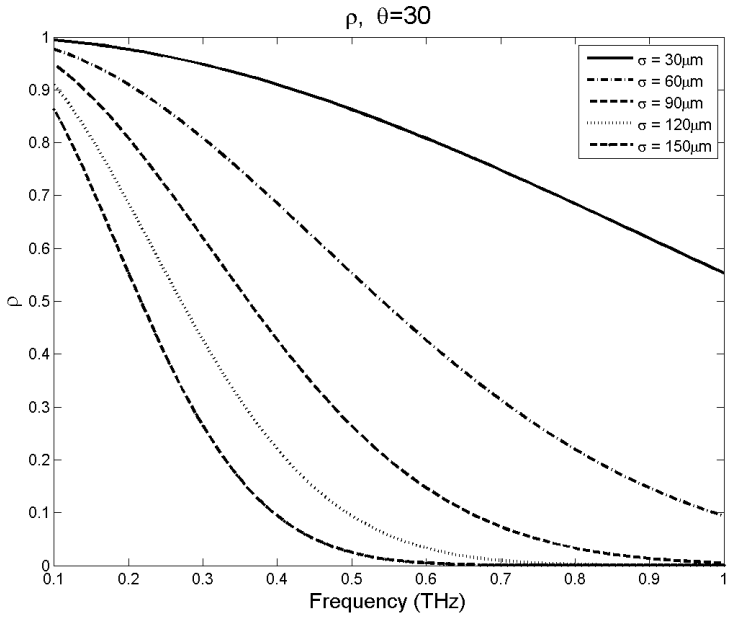


Figure 3-2. Normalized mean specular direction signal strength at 0.1THz to 1THz (Rayleigh roughness factor)

Variance from the expected mean of the signal can also be calculated using equations (14) and (15). Table 3-1 compiles the general expression for expected mean and variance of the scattered signal, and those for Gaussian random rough surface. Given the statistical roughness parameters σ and *l* of random Gaussian distributed rough surface, expressions in Table 3-1 allows to evaluate expected mean signal and variance from rough surface scattering at THz wavelength.

Table 3-1. Expected Signal Strength and Variance of Scattered Wave from Random Surface

| | |
|---|---|
| Specular direction mean roughness factor | $< \rho_{spec} > = \exp\left[-\frac{1}{2}\left(\frac{4\pi\sigma \cos\theta_1}{\lambda}\right)^2\right]$ |
| Variance D of one-dimensional general surface | $D\{\rho\} = \frac{F^2}{2L}\int_{-L}^{L} e^{iv_x\tau}[\chi_2(v_z,-v_z) - \chi(v_z)\chi^*(v_z)]\, d\tau$<br>$\tau$ = distance between any two point on the surface (in x) |
| Variance D of two-dimensional general surface | $D\{\rho\} = \frac{F_3^2}{A^2}\int_0^{\infty}\int_0^{2\pi} e^{i(v_x\tau cos\varphi + v_y\tau sin\varphi)}[\chi_2(v_z,-v_z) - \chi(v_z)\chi^*(v_z)]\, \tau d\tau d\varphi$<br>Or equivalently,<br>$D\{\rho\} = \frac{F_3^2}{A^2}\int_0^{\infty} \boldsymbol{J_0}(v_{xy}\tau)[\chi_2(v_z,-v_z) - \chi(v_z)\chi^*(v_z)]\, \tau d\tau$ |
| <u>Gaussian Surface Profile</u> | |
| Moment generating function | • 1D: $\chi(v_z) = \exp(-\frac{1}{2}\sigma^2 v_z^2)$<br>• 2D: $\chi_2(v_z, -v_z) = exp[-\sigma^2 v_z^2(1-C)]$<br>where $C = e^{\frac{-\tau^2}{T^2}}$, T is correlation length analogous with *l* |
| Exponential Expansion of $\chi$ | $\chi_2(v_z, -v_z) = e^{-\sigma^2 v_z^2}\sum_{m=0}^{\infty}\frac{g^m}{m!}e^{\frac{-m\tau^2}{T^2}}$<br><u>where</u><br>$\sqrt{g} = v_z\sigma = 2\pi\frac{\sigma}{\lambda}(cos\theta_1 + cos\theta_2)$ |
| Variance in 1-D surface | $D\{\rho\} = \frac{\sqrt{\pi}F_2^2 T}{2L}e^{-g}\sum_{m=0}^{\infty}\frac{g^m}{m!\sqrt{m}}e^{\frac{-v_x^2T^2}{4m}}$ |
| Variance in 2-D surface | $D\{\rho\} = \frac{\pi g F_3^2 T^2}{A}e^{-g}\sum_{m=0}^{\infty}\frac{g^m}{m!\sqrt{m}}e^{\frac{-v_{xy}^2T^2}{4m}}$ |

3.2. Kirchhoff Scattering Theory and Roughness in the THz Region

The g number from (20) represents the ratio of wavelength and roughness measurement, and allows the application of KA over broad range of wavelength and roughness parameter. The value of g is more appropriate description of roughness at a specific wavelength. Value of g <<1 implies variation in the surface profile is much smaller than the wavelength and the surface is considered smooth. g~1 is considered moderately rough surface, while g>>1 implies the 'very' rough surface. For height deviations from 30μm to 150μm, in 0.1THz to 1THz region, the value of specular direction g spans from smooth to rough region. (Figure 3-3). Figure 3-2 and Figure 3-3 show that for higher value of g at shorter wavelength, the mean expected signal amplitude decays.

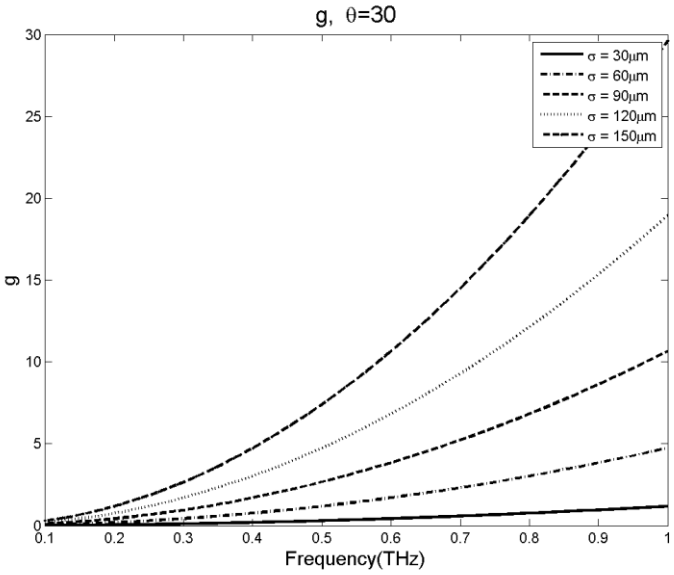


Figure 3-3. g number in the THz region for roughness height of 30um to 150um at 0.1THz to 1THz

Variances of the signal presents a different problem. Random value of the signal with the variance calculated from equation (14) or Table 3-1 will manifest as noise in the measured THz signal of an image pixel. Using Table 3-1, the variance of the signal at the specular direction can be computed. Such variance is a function of both normal height deviation from the mean σ and the

correlation length l of the surface. Figure 3-4 plots the normalized variance for fixed l=80μm, varying height deviation (a) and fixed height deviation at σ=30μm, and varying l, over the range of 0.1THz to 1THz. Larger correlation length actually predicts greater variance in the specular direction. At much shorter *l* (compared to THz wavelength ~ 500 μm), the signal tend to scatter diffusely and less magnitude of variance are predicted.

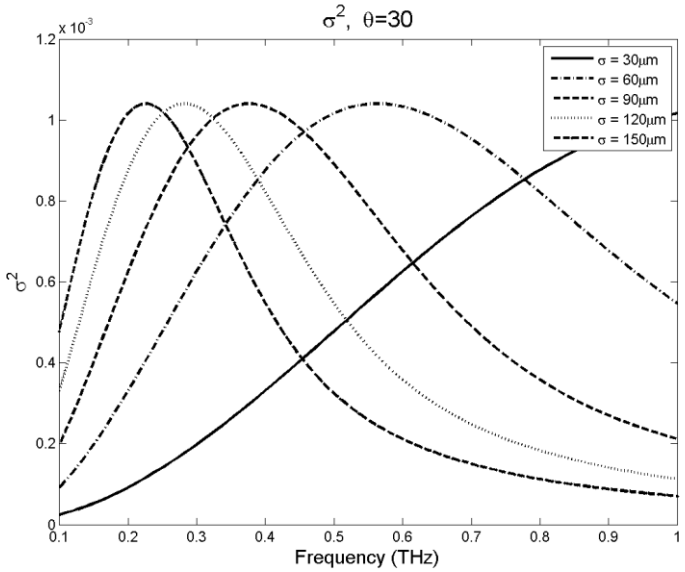


(a)

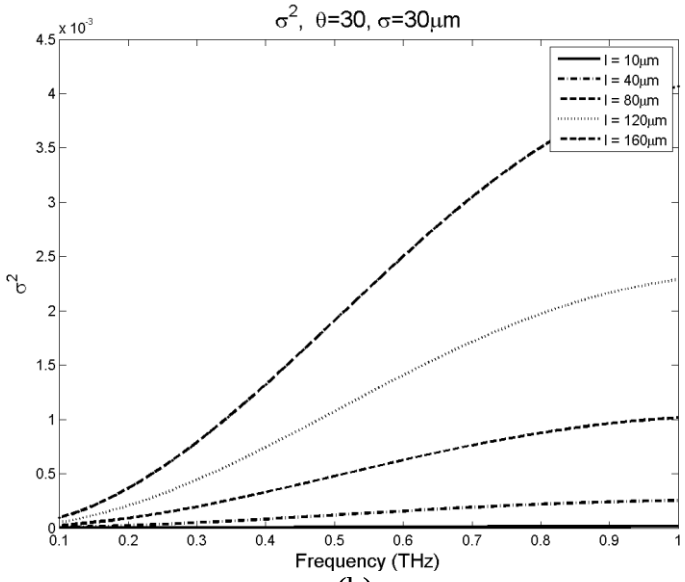


(b)

Figure 3-4. Normalized variance of specular direction signal at 0.1THz to 1THz, for a. fixed *l*=80μm and b. fixed σ=30μm

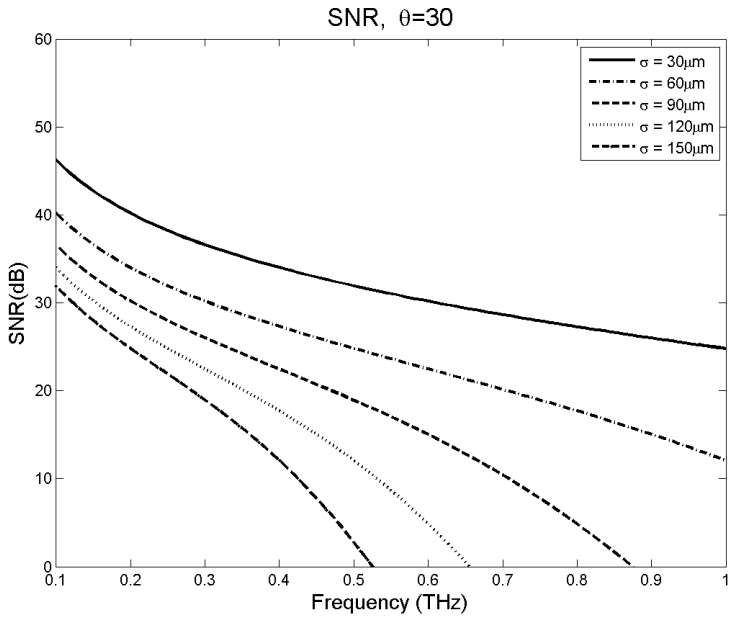


(a)

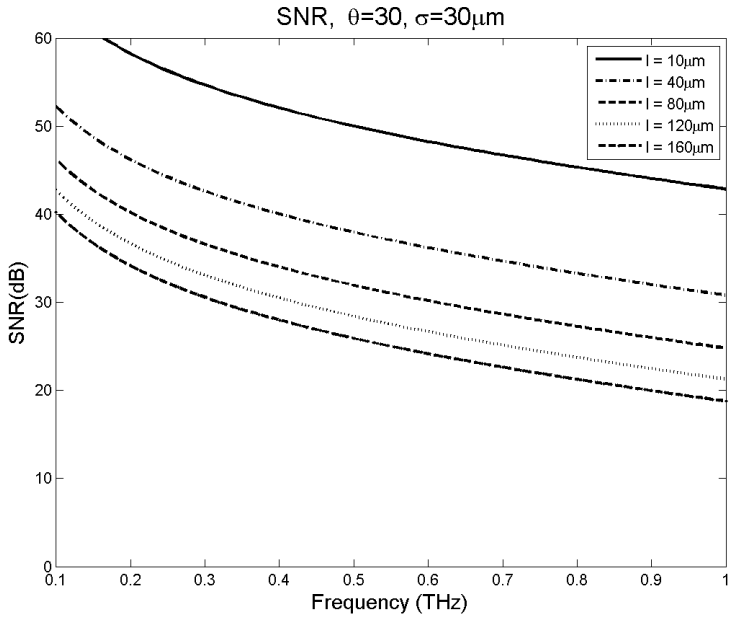


(b)

Figure 3-5. Signal to Noise Ratio (SNR) imposed by the presence of roughness at 0.1THz - 1THz for (a) fixed $l$=80μm and (b) fixed σ=30μm

Local maxima occurs at THz region for the varying value of σ and fixed value of $l$=80μm that correspond to typical roughness parameter of the skin. It is noted that while σ directly corresponds

to physical dimension of roughness, *l* is a less straightforward parameter and are difficult to measure or produce. The signal to noise ratio (SNR) can be calculated from expected signal strength ρ and the variance σ. Note that SNR is also a function of illuminated area, A; sharper the focused spot, it is more likely that the wave scatters to non-specular direction and SNR decreases. Figure 3-5 plots SNR as a function of frequency and height deviation with *l*=80μm, and a constant illuminated area of 3mm x 3mm.

The validity of the Kirchhoff Approximation method is restricted to loosely defined "gently undulating surface" – surfaces whose rough features have radius of curvatures sufficiently larger than the wavelength $L>>\lambda$ and large illumination area $A >> \lambda^2$. Simplified expression is possible for perfectly conducting surface. Derivation of results in Table 3-1 also assumes for uniform illumination over a perfectly conducting surface, while shadowing, multiple scattering and mutual interaction of irregularities are ignored. Currently in most applications, including most THz TDS and reflection mode sensing systems, active THz illumination is done under a focused aperture. On the other hand, broadband THz illumination from ultrafast current from photoconductive switch is inherently limited to pulsed operation with a large bandwidth, while the solutions obtained above are derived at a single wavelength. Experimental validation is required to test if the approach in this section works in the THz region. While there are many different THz illumination and detection methods, the validity of Rayleigh roughness factor from KA is investigated by Piesiewicz et al. in [30] for a focused and pulsed THz incident wave on a plaster target, to give good agreement with predicted decrease in signal over the range of 0.1THz to 1THz range. The experimental measurement of reflectivity from TE and TM polarized incidence beam is consistent with those predicted by the Fresnel Equation and equation (19). [30]

3.3. Rough surface imaging: characterization of the direct detection system

The variance of the signal can be directly observed in an image of rough, otherwise uniform surface by the variance of the pixel signal intensity. Four metal plates are prepared with different degree of roughness by polishing the surface with Silicon Carbide sandpaper. Roughness of the sandpapers are commonly reported in Grit, which labels the average particle size composing the sandpaper surface. Table 3-2 compiles the Grit value of the sandpapers used in the preparing the brass plate.

Table 3-2. Average particle size for Silicon Carbide Sandpaper Grit Values

| Sample number | Grit (US unit) | Average particle diameter (μm) | Height deviation σ (μm) | Correlation length (μm) | THz Image SNR (dB) |
|---|---|---|---|---|---|
| 1 | 600 | 15 | 1.77 | ~ 80 | 54 |
| 2 | 300 | 36 | N/A | N/A | 54 |
| 3 | 180 | 78 | N/A | N/A | 52 |
| 4 | 80 | 265 | 15 | < 50 | 44 |

Preparation of rough surface is performed with MultiPrep$^{TM}$ precision polisher with reported minimum material removal depth precision of ±2μm (Allied High Tech, CA). Each sample is leveled to the polishing surface (±2μm) and polished with separate rotation of the sample, polishing surface (sandpaper), and movement of the polishing head. The polished surfaces are not expected to have same degree of roughness as the sandpaper. In fact, the polishing movement renders the surface much smoother than the particle size.

Measurement of the actual surface profile was necessary to correctly determine the parameters pertinent to expressions in Table 3-1. A 2-D height profile map is measured with 5μm diameter

probe over 2.5mm x 2.5mm area. Measurement of height profile for sample 1 and 4 are reconstructed to a 2-D image in Figure 3-6 and Figure 3-8, respectively. Statistical parameters of profiles in x and y axis were within 10% difference.

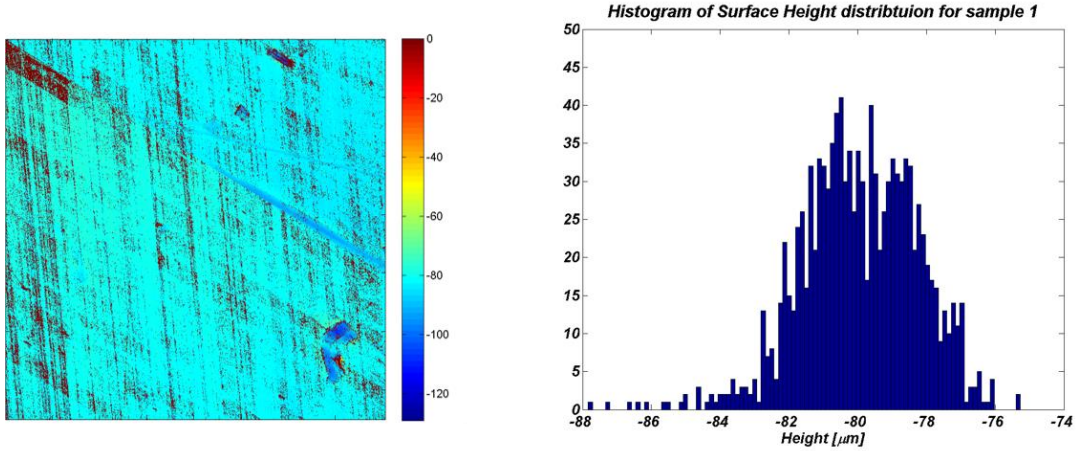


Figure 3-6. Reconstructed image of height profile and distribution of sample 1

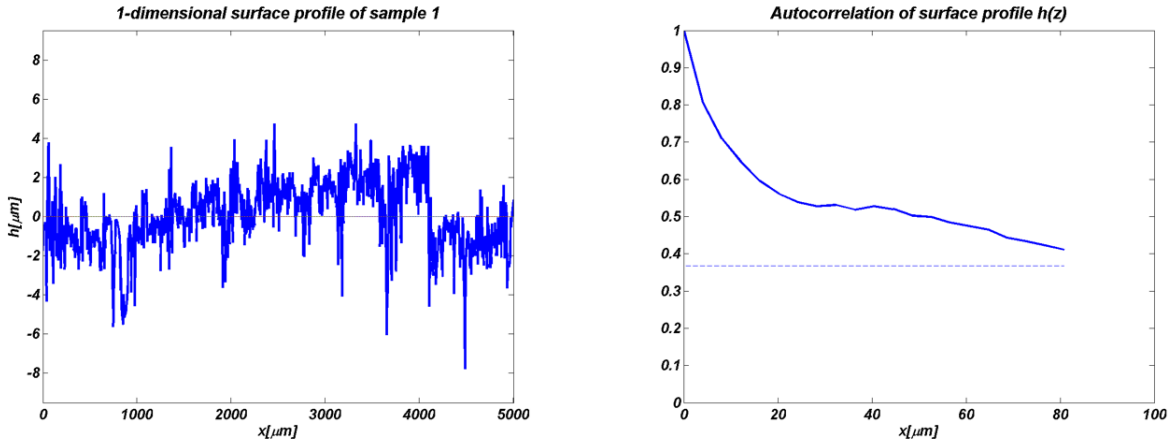


Figure 3-7. Height profile in x and its autocorrelation function of sample 1

For the most smooth surface (sample 1) polished with 600 Grit sandpaper, a histogram of height distribution shows almost symmetric distribution of height (Figure 3-6). The mean and median of the distribution are within 5% difference for samples whose measurements are available, and for each sample, the mean height is set to zero. The autocorrelation function of the height profile is computed and plotted in Figure 3-7. Correlation length $l$ is computed to be the distance in x or y

when the autocorrelation function has decayed to 1/e. For sample 1, standard deviation σ from the mean was 1.77μm and the correlation length *l* is found to be near 80μm. Sample 1 is highly smooth at THz wavelength with g number of 0.0185. THz image acquired with 0.5mm x 0.5mm pixel size are compared with visible images of the target shown in Figure 3-10. While high-degree of randomness of the polished profile is desired, periodic toolmarks and grinding patterns are observed in both visible and THz images, while delineated more strongly in THz images. (Figure 3-10 and Figure 3-11). It is noted that the apparent regularity in the surface profile is accounted in the computation of correlation length, while the computation of signal to noise ratios in the THz images is independent of the corresponding periodicity observed in the images.

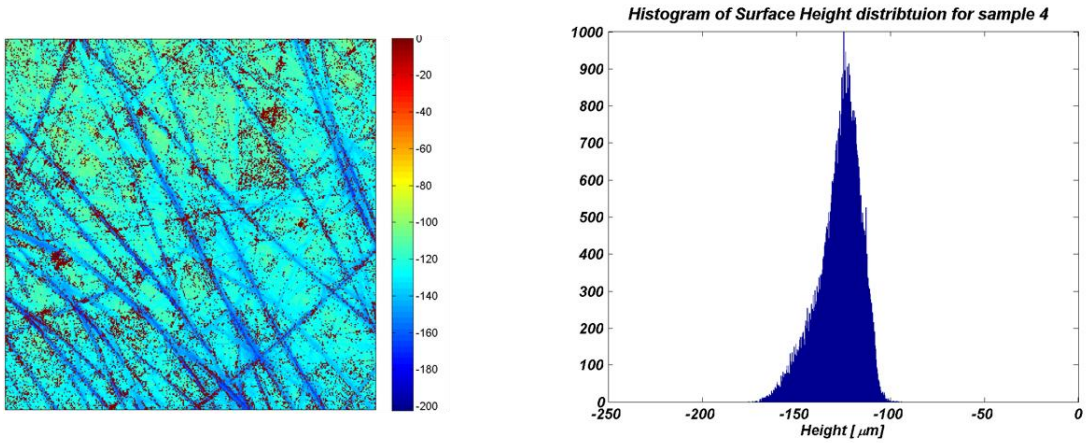


Figure 3-8. Reconstructed image of height profile and distribution of sample 4

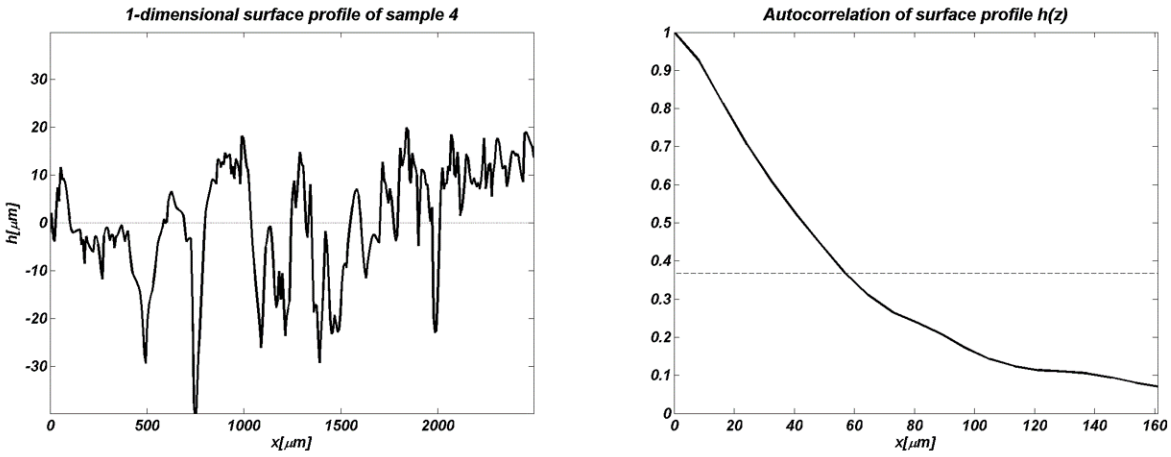


Figure 3-9. Height profile in x and its autocorrelation function of sample 4

In comparison, reconstructed height profile image of the roughest sample (4) and its distribution, autocorrelation function, and corresponding THz and visible images are shown in Figure 3-9 and Figure 3-11, respectively. For sample 4, the distribution of height becomes more asymmetrical. Standard deviation from the mean increased to σ=15μm and the correlation length is reduced to <60μm. THz images of sample 4 shows different signal range compared to that of sample 1. The variance from the mean signal in each sample is computed and signal to noise ratio is computed.

$$SNR_{scatter} = \frac{\mu_{THz}^{\ 2}}{\sigma_{THz}^{\ 2}} \qquad 21$$

where μ is the mean signal in the image and σ is the standard deviation, as can be seen in Figure 3-12. The variance and the signal-to-noise ratio of the signal in the image is computed for all 4 samples. The first three samples achieved the system's noise-limited SNR of 54dB. Only sample 4 showed degradation in SNR below 50dB. Because of the system's large signal bandwidth and polarization sensitive detection method, expected SNR by the direct detection system may not be directly computed from weighted average of expected SNR using Table 3-1 and Figure 3-5.

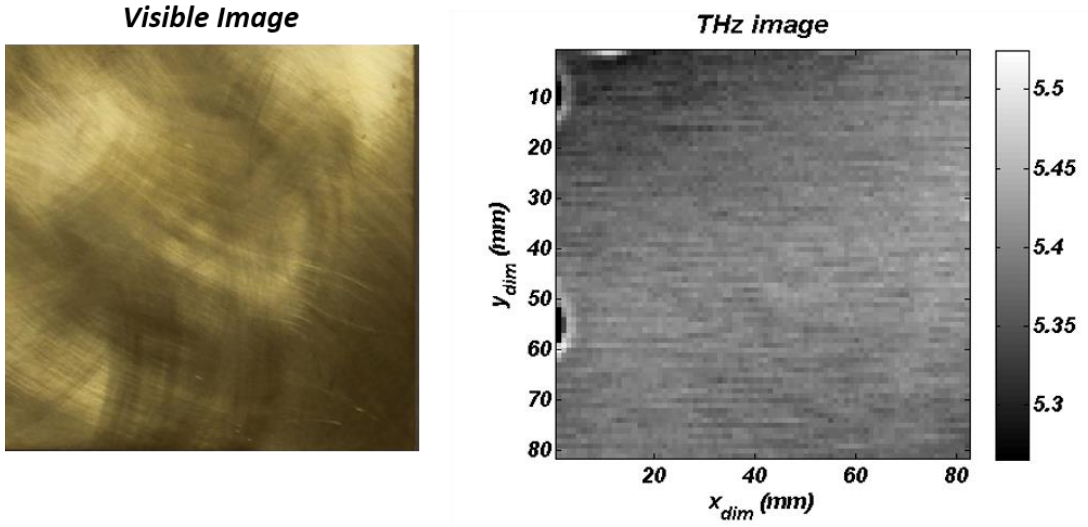


Figure 3-10. Visible and THz images of target with g=0.0175 at 0.6THz (sample 1)

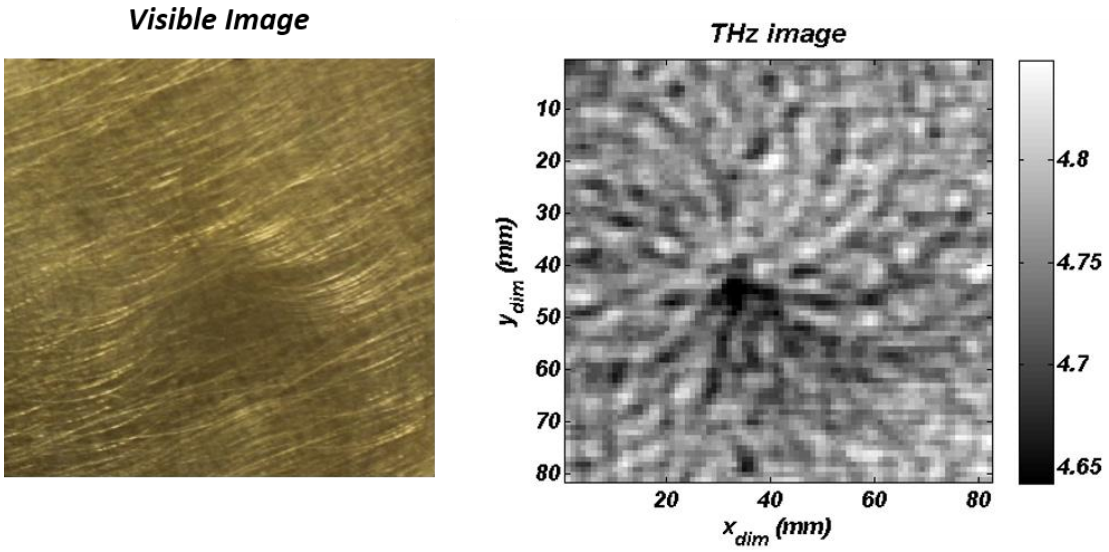


Figure 3-11. Visible and THz images of target with g=0.101 at 0.6THz (sample 4)

Observation of variations of signal from roughness for sample 1-3 are obscured by the maximum system SNR. While height deviation in the sample 4 is still considered smooth from its g-number below 0.3, the decreased correlation length is suspected to contribute to SNR decrease of 10dB. SNR at the detection band of 0.4THz to 0.7THz agrees within ±6 dB with that expected by Table 3-1 and Figure 3-5, which expects SNR of 40dB±3dB at the detection band of 0.4THz to 0.7THz. The result of roughness measurement characterization can be interpreted as indirect experimental validation of SNR limit set rough surface scattering. The full range of KA's validation in the THz region can be investigated in the future study with surface prepared with more severe roughness.

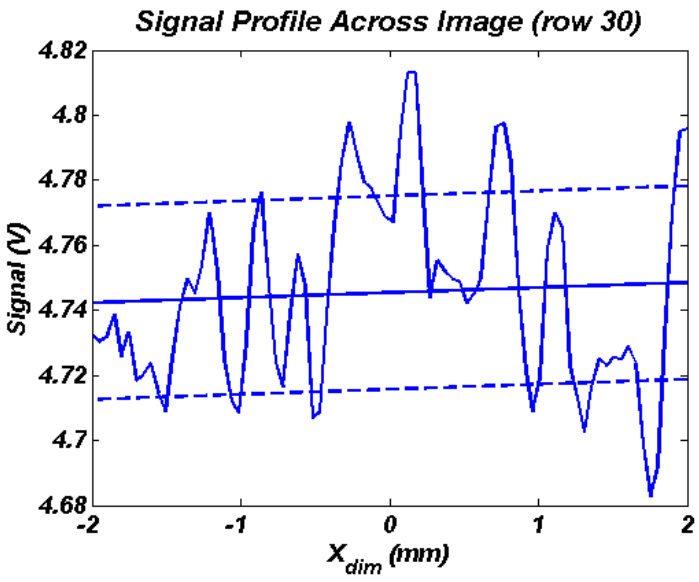


Figure 3-12. Signal profile of THz image, with signal mean and standard deviation

3.4. Smoothness of skin

Biological tissues, especially skin, are highly inhomogeneous medium. Surface topology of the skin differs by the function of the tissue (skin), location, dermatologic condition and composition of organ features such as sweat glands, wrinkle, etc. Many literatures attempted to characterize roughness of skin. Depending on the location, skin is known to have mean height deviation from 15 μm (forearm) to as much as 120 μm (soles of the heel).

Table 3-3. Measurement of Typical Skin Height Profile in Root Mean Square of Height Deviation ($R_{rms}$)

| | |
|---|---|
| Typical Height deviation (σ) | 10-40 μm [31]<br>15-120 μm [32] |
| Correlation length (*l*) | Typical: 80 μm<br>Psoratic: 180 μm [33] |

Above parameters of roughness of skin puts it in the “moderately smooth” surface, having g ~ 1 over the range of entire THz region. The correlation length of the skin is also measured by [33]. Under certain condition, the correlation length ($l$) can also change. As the roughness of the skin approaches close to 100um, the skin should be considered “rough” surface with g ~ 10 at frequencies higher than 0.5 THz. At such case, the roughness of the tissue will play significant role in signal-to-noise ratio.

# Chapter 4 Construction and Characterization of Beam-Scanning System

As discussed in Chapter 1, applications for THz medical imaging have proliferated rapidly in recent years due to advancements in source/detector technology and vigorous application development. While considerable effort has been applied to improving source output power and detector sensitivity, less attention has been devoted to improving image acquisition method and time. The majority of THz medical imaging systems in development typically acquire pixels by translating the target of interest beneath a fixed illumination beam. While this single-pixel whiskbroom methodology is appropriate for *in vitro* models, it is unsuitable for *in vivo* large animal and patient imaging due to practical constraints. In this section, an improved version of scanned beam imaging system is presented. Image acquisition by beam scanning reduces image acquisition time while keeping the source, target and detector to remain stationary.

The active, spinning mirror based THz imaging system architecture is shown in Figure 4-1 (a),(b),(c). The system employs a spinning polygonal mirror and a set of high-density polyethylene (HDPE) objective lenses. An identical THz source and detector device described in Chapter 1 is used, operating at a center illumination frequency of 525GHz with ~125GHz of 3dB bandwidth.

## 4.1. System Construction

Shown in Figure 4-1(a), emitted THz radiation is collected and collimated by a 2" clear aperture, 50.8 mm effective focal length (EPL) 90$^{o}$ off-axis parabolic mirror (OAP1). The collimated beam with approximately 20 mm diameter interfaces with a 76 um mylar beam splitter with a reflectivity-transitivity ratio of ~50/50 in the illumination band. The beam splitter shows reflectivity-transitivity ratio of ~50/50 at a 45 degree incident TE polarized beam angle. Each line scan in y-direction is achieved by the rotation of the polygon mirror, as shown in Figure 4-1(b).

Scanning in the +x direction is achieved by linearly translating the polygonal mirror and scanning lens together as shown in Figure 4-1(c).

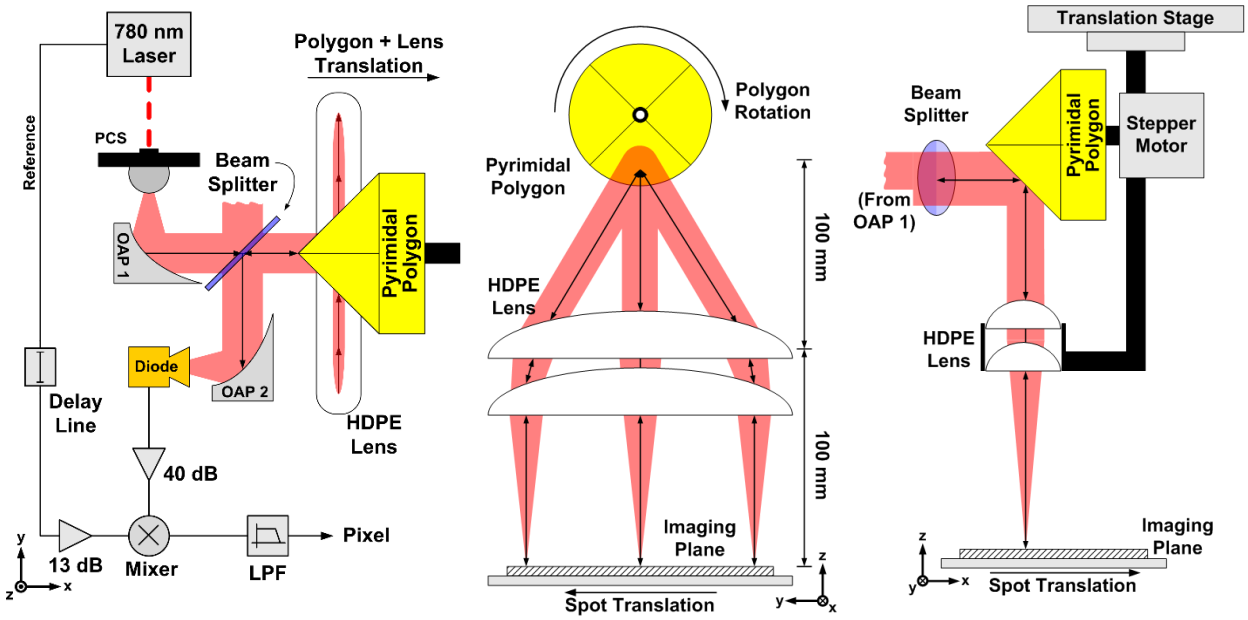


(a) (b) (c)

Figure 4-1. Spinning mirror system design and construction.
(a) top down (b) front, and (c) sideview

Approximately 50% of the collimated THz beam power from OAP1 is directed to a 62.5 mm, 90 degree pyramidal polygon mirror. A pair of HDPE convex lenses, each with a 25.4 mm x 101.6 mm clear aperture and focal length of 190 mm, refracts the scanning beam to normal incidence across the imaging plane. The polygon is positioned at the effective focal point of the HDPE lenses such that the beam strikes the target at normal incidence for all scanning angles of the polygon. 2-D images are acquired by translating the polygon and the lens together in ±x direction while acquiring y-direction line scan. The addition of the second lens achieves superior beam focusing and wider scanning angles at the expense of multiple Fresnel reflection losses. In contrast, a single bi-convex design will have shorter radius of curvature and will produce more severe spherical aberrations. The focal length of the scanning objective was measured to be ~ 100 mm where the

deviation from the ideal 95 mm (190 mm/2) is most likely due to the non-zero separation between the lenses. The focused illumination beam is reflected back to the lens at a normal, retracing the illumination path. At the beam splitter, 50% of the returned beam is directed to the second OAP, which focused collected THz beam to the feedhorn of a zero-bias Schottky diode detector.

## 4.2. System Characterization

### 4.2.1. Illumination Uniformity

The scanning angle of the polygon is confined within ±15 degrees where paraxial approximation is valid and uniform angular speed scanning results in uniform linear translation of the illumination spot over the FOV. Imperfections in the polygonal mirror and scanning objective lens fabrication introduces minor changes in the illumination strength over the imaging field. Illumination uniformity is inspected by imaging a flat, uniform calibration target (polished aluminum plate) placed at the imaging plane. The return signal strength profile is plotted in Figure 4-2(b). Sharper drops in signal at the x-extremes are due to signal asynchronization between the THz pulse and the reference pulse. The overall optical path length of the rectified THz pulse changes due to translation of the polygon and the lens and results in temporal misalignment. For acquisition of a large FOV, such signal asynchronicity can be addressed by dynamically adjusting the effective path length of the reference pulse. Although it was not necessary in this study, measurements such as those shown in Figure 4-2(a) can serve as a calibration field for image post-processing.

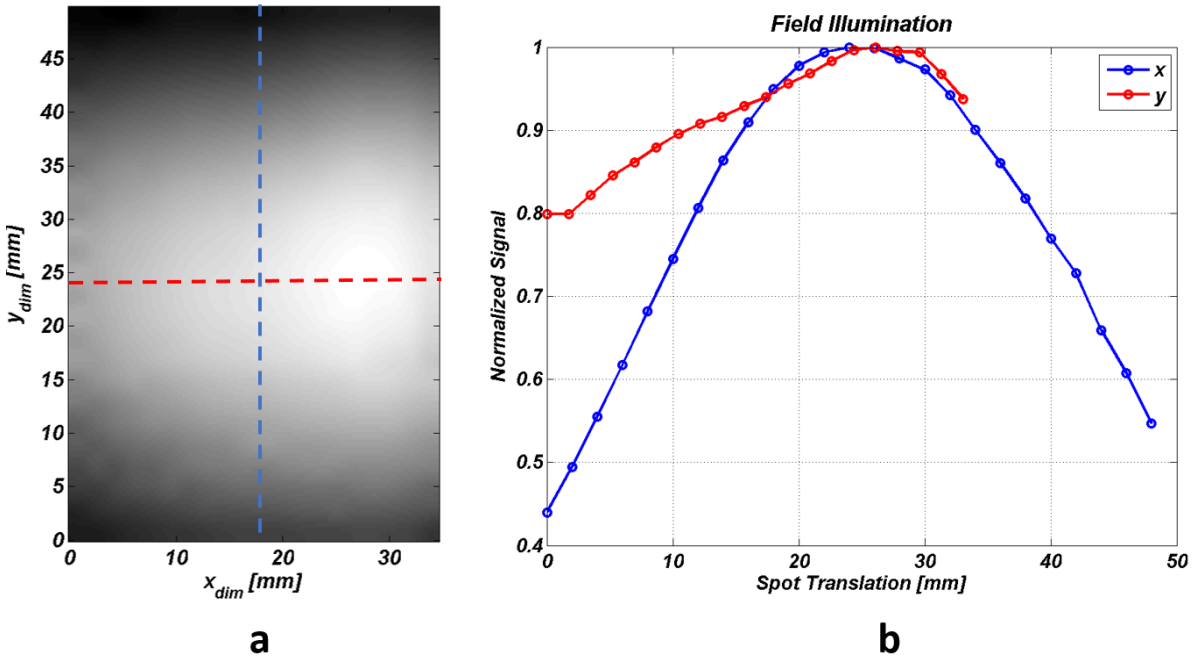


Figure 4-2. Flat imaging field illumination strength characterization of spinning-mirror system.
a. Field illumination strength over the imaging field.
b. Normalized illumination strength profile by scan and translation.

### 4.2.2. Spot Size

For the imager to operate as designed in Figure 4-1(b), it is crucial that the polygonal mirror facets are aligned to the focal plane of the HDPE lens and the scanning objective behaves like a thin lens. This alignment is important in ensuring the retro-directive behavior and paraxial operation over the limited cone of scanning angles allowed by the lens clear aperture. Minimum spot size is achieved at the beam waist at the focal distance of the lens. Therefore, the imaging plane is formed at focal plane of the scanning objective. The spot size and profile is measured by knife-edge method described in chapter 1. Spot translation as a function of polygon rotation is also characterized in Figure 4-3(b). A knife edge target is scanned over the spot locations for polygon rotation angles from -10 deg to +10 for every 1$^{o}$ step with 0$^{o}$ positioned such that reflected beam is normal to the lens optical axis.

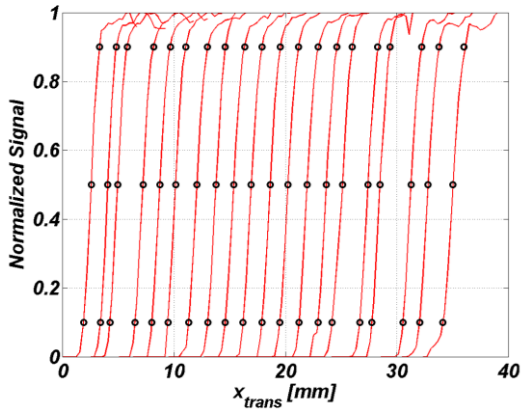


(a) Knife edge response

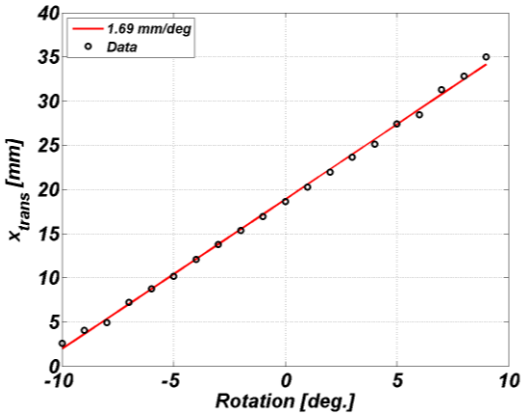


(b) Spot translation as a function of mirror angular displacement

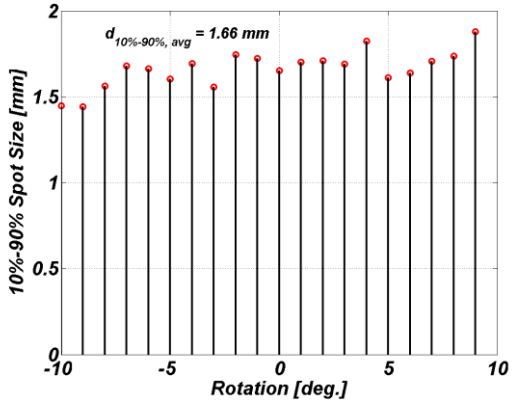


(c) Spot size as a function of spot location (polygonal mirror angular displacement)

Figure 4-3. Spot size and beam translation characterization at the imaging plane

The normalized knife edge response over the distance of 38 mm in polygon scanning direction is plotted on Figure 4-3(a). Three black markers on each curve denote 10%, 50%, and 90% point for the THz irradiance. 50% crossover point in the knife edge plot represents the approximate center of the focused beam. Spot translation distance as a function of polygon rotation is plotted in Figure 4-3(b). The linear fit confirms paraxial approximation and the spot moves 1.695 mm on target per degree rotation of the polygon. The measured spot size agrees with the 1.5 mm expected spot size using Gaussian beam methodology [34]. 10%-90% knife edge spot size data are plotted in Figure

4-3(c), with a ~1.66 mm average spot size across the 20 degrees of polygon sweep. These results confirm that the polygonal mirror facets are within the focal range of tested ± 10 deg. of scanning, and the set of scanning lenses behaves as a thin lens with an effective focal length of ~100 mm in this application.

4.2.3. Depth of Field

Compared to short focal distance and high numerical aperture of OAP objective mirrors, the combined effect of larger focal distance of HDPE scanning objectives and normal illumination angle incidence produced very large depth of field (DOF) measurements. To measure the DOF, a uniform aluminum target was translated in the ±z direction (denoted in Figure 4-1) to measure signal strength as a function of z, for each polygon rotation position in the ±10 deg range. The measurement is taken at $1^{o}$ rotation step size. The ensemble of DOF measurements for each angle is plotted in Figure 4-4(a). A Gaussian fit has been calculated for each polygon rotation and is superimposed on the data and the effective DOF is defined as the range of translation that retains 50% or more of the maximum signal. Figure 4(b) plots the DOF over the range of ±10 deg scan angles. This set-up achieves at least 25 mm of DOF, and is commensurate with the computed Rayleigh length of 27.8 mm using the focal distance of the objective lens and Gaussian beam theory. The drop in signal in ±z translation is most likely due to the signal asynchonization between the rectified THZ pulse and the reference pulse, suggesting that the actual DOF may be closer to the computed Rayleigh length. We suspect the asymmetry in the computed DOF over the scan angle may be due to imperfect alignment of the polygon and lens orientation

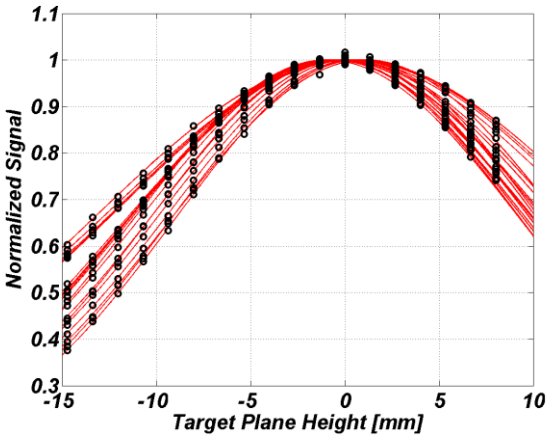


(a) Normalized signal strength versus target plane depth

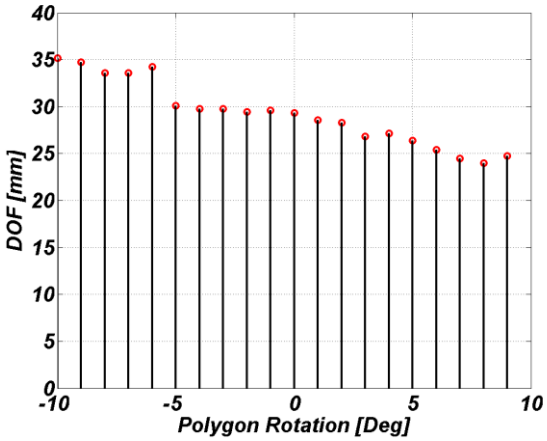


(b) DOF by each rotation angle

Figure 4-4. Depth of field (DOF) measurement by rotation angles.

This broad DOF is advantageous in practical clinical applications for the following reasons: 1): The target does not have to be critically aligned within the narrow z range before imaging. Small error in target position is allowed to obtain a focused image. 2): Mild tissue curvature can be tolerated, particularly in tissue geometries such as that of the eye. Improved DOF minimizes changes in the dynamic range of pixels at different locations due to the target's curvature, and flattening of the sample may no longer be needed. These benefits are especially critical in clinical imaging of the cornea and burn wounds where contact measurements are discouraged due to discomfort and sterility

## 4.3. Imaging Result

A 4cm by 4cm copper pattern on dielectric substrate is used as a calibration target to test the imaging system's performance.(Figure 4-3). The image is obtained with a 1 mm x 1 mm pixel size

and a 35 mm x 35 mm FOV at a standoff distance of ~ 100 mm. The target pattern was chosen to evaluate the spatially invariant performance of the imaging system.

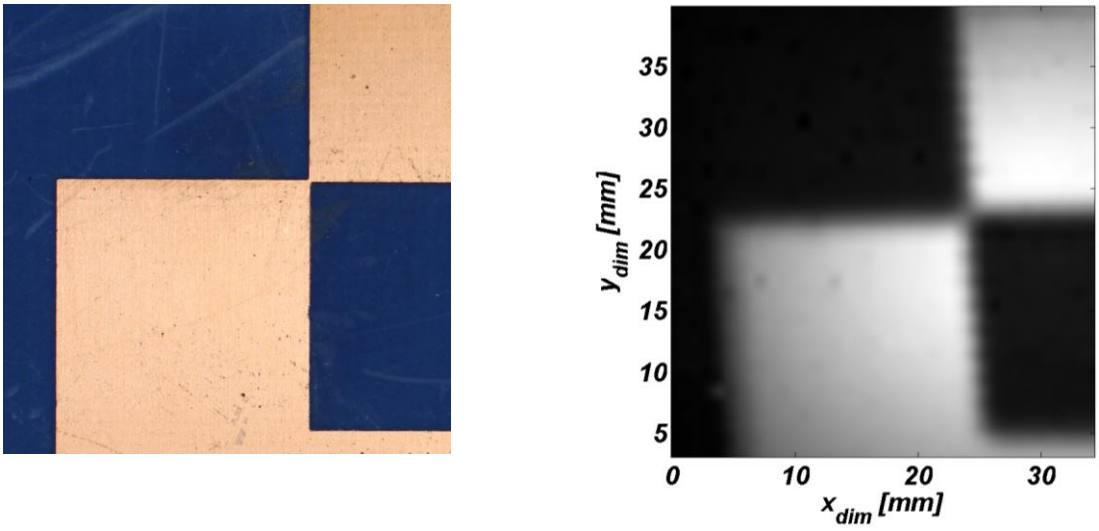


(a) Visible (b) THz

Figure 4-5. Characterization target imaging results. a. Visible image. b. THz image

Images of animal *ex vivo* samples containing adipose fat and muscle tissue (prosciutto slices) are shown in Figure 4-6. The aim of this study was to acquire THz imagery with sufficient contrast between reflective tissue components with water content (muscle) and non-reflective adipose fat tissue. Figure 4-6-1(b) and Figure 4-6-2(b) are acquired with a FOV of 35 mm x 25 mm and 35 mm x 35 mm, respectively, using a 1 $mm^2$ pixel size. The THz images show defined contrast between reflective muscle tissue and non-reflective adipose tissue. Delineation of less obvious features which are overlooked by visible inspection are also captured with THz imaging. Although this system operated at a narrow dynamic range of less than 4mV of signal after amplification, these images show comparable contrast between different tissue types as those obtained by conventional sample-translation methods and higher dynamic range. Images suffer from non-

uniform illumination across the imaging field. A flat calibration field can be used to normalize THz imagery to the field illumination strength to obtain better images.

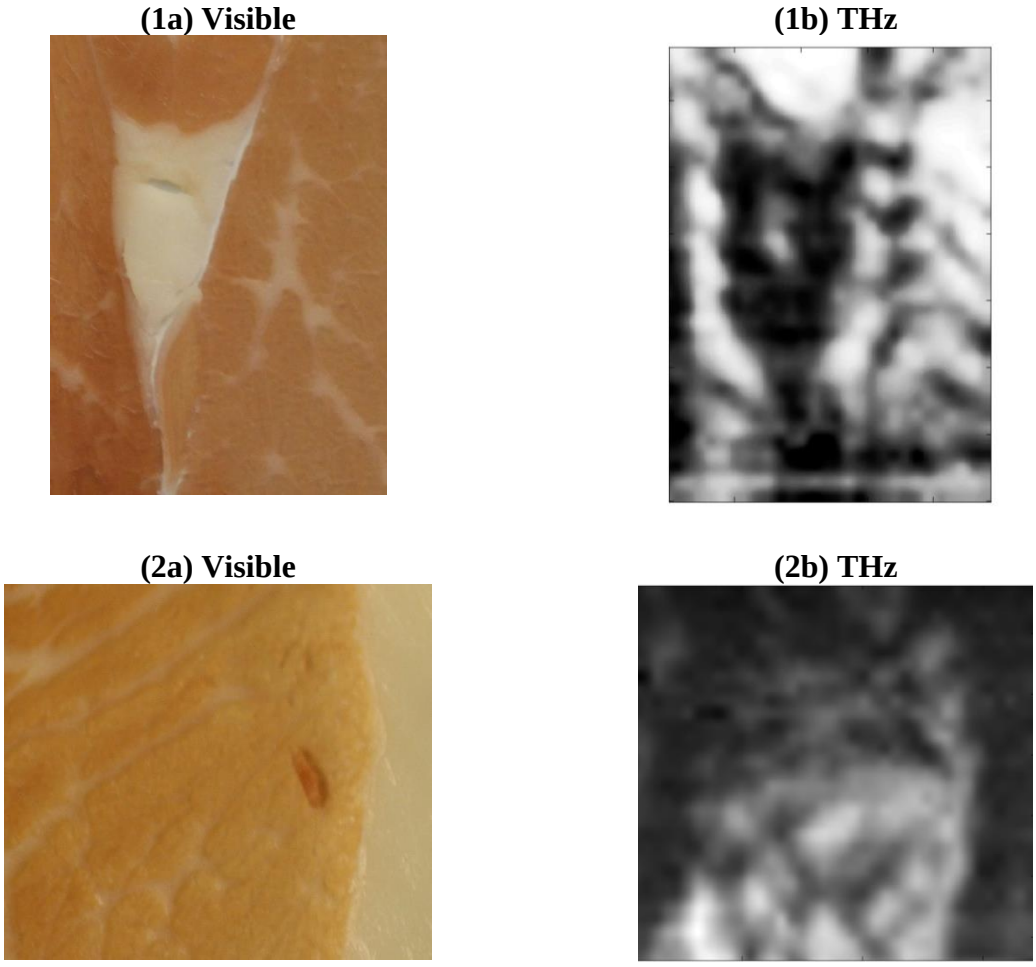


Figure 4-6. Ex-vivo sample imaging results, using different part of a prosciutto slice.

4.4. Discussion: Toward Clinical Application

The addition of a second scanning objective achieved a smaller spot size closer to the diffraction limit, compared to that obtained with the first version of this system. The lenses produced uniform spot translation and spot size across the imaging field, and thin lens approximation is valid in this application. Reduced focal distance between the polygon and the lens requires a greater scan angle to cover the same FOV compared to a single lens set-up. While a larger scan angle reduces angular

rotation error due to motor operation, the required scan angle approaches near paraxial approximation limit. There is a trade-off between using dual lenses of lesser curvature versus using a single lens with higher curvature. The dual lens suffers from reduced signal strength and dynamic range, as it is characterized by four air/dielectric interfaces subjected to Fresnel losses. However, the multiple lenses set-up keeps the off axis aberrations minimal at the expense of Fresnel loss, since the radius of curvature of the lenses is kept small while achieving sharper focus. The dual lens design also allows for greater paraxial limits compared to using a single lens with higher curvature and avoids geometric aberrations at a larger FOV.

The large DOF achieved by smaller numerical aperture of lens design combined with normal incidence angle present great utility in practical clinical imaging procedures. Small misalignment of the target to the optimal imaging plane can be tolerated. Imaging of tissues with minor curvatures can be performed without having to flatten the target. Larger FOV can be easily implemented with a larger scanning objective lens and appropriate THz and reference signal path length synchronization. Currently, image acquisition time is limited by open loop, non-synchronized operation of the polygonal mirror motor, motorized translation of the stage, and the sample acquisition rate of the analog-to-digital converter (ADC). There is a large room for improvement in more sophisticated instrumentation control and synchronization to approach in acquisition time that is ultimately limited by SNR of the detection scheme. At the current pixel integration time of 3 ms, upto 300 pixels per second is possible, which will acquire 50mm x 50mm image with 0.5mm x 0.5mm pixel size in 30 seconds. However, the lens-based system indeed suffered from weak THz signal and low SNR compared to the OAP mirror-based system. At this stage, maximum image contrast range is desired by increasing integration time, given the same THz source power and detector sensitivity.

## Further remarks and Summary

Three key engineering aspects are visited in designing and implementing THz imaging system for medical application. Chapter 2 investigated how electromagnetic wave at THz frequency behaves in off-axis parabolic (OAP) mirror based optical system. Component orientations and focusing /collimating performance of OAP mirrors need to be considered to achieve desired target illumination and effective coupling of THz wave to detectors. The findings in this section provide a guideline to novel optical system designs effort. Chapter 3 focused on the application of well-known scattering theory in THz wavelength, particularly to explore how skin roughness plays a role in medical imaging application. A characterization measurement of polished brass target confirmed expected SNR degradation in a broadband direct-detection system. Nonetheless, validity of using the Kirchhoff solution to predict SNR at THz region shall be rigorously tested with a narrow band illumination. Direct comparison of THz imagery with profilometry data of tissue targets (i.e. skin, cornea) can establish proper THz scatter models toward clinical application. An improved scanned beam THz imaging system for medical applications is presented in chapter 4, whose design goal is to acquire THz imagery of a stationary target at the normal incidence across the entire imaging field. By the dual-lens design, a large depth of field affords significantly improved tolerance to target misalignment and curvature. This study lays a groundwork for in-vivo THz imaging applications in the burn wound diagnosis and corneal hydration sensing, as both applications present needs for design of clinically viable systems, shortened image acquisition time, and robust signal acquisition method. Lastly, although outside the scope of this manuscript, both theoretical and experimental investigation of THz interactions with various chemical states of water in tissue remain an important task in understanding THz-tissue interactions and how THz

imagery generate contrasts. Such aspects will be part of author's continued course of study to establish physical principals for medical diagnostics model, pertinent with physiology.

# References and Bibliography


1. Tonouchi, M., *Cutting-edge terahertz technology.* Nat Photon, 2007. **1**(2): p. 97-105.
2. Williams, B., *Terahertz quantum-cascade lasers.* Nature Photonics, 2007. **1**: p. 517 - 525.
3. Bennett, D.B., et al., *Terahertz sensing in corneal tissues.* Journal of Biomedical Optics, 2011. **16**(5): p. 057003-8.
4. Taylor, Z.D., et al. *THz imaging based on water-concentration contrast*. 2008. Orlando, FL, USA: SPIE.
5. Brown, E.R., et al. *THz imaging of skin tissue; Exploiting the strong reflectivity of liquid water*. in *Infrared Millimeter and Terahertz Waves (IRMMW-THz), 2010 35th International Conference on*. 2010.
6. Pickwell, E., et al., *In vivo study of human skin using pulsed terahertz radiation.* Phys Med Biol, 2004. **49**(9): p. 1595.
7. Pickwell, E. and V.P. Wallace, *Biomedical applications of terahertz technology*. Journal of Physics D: Applied Physics, 2006. **39**(17): p. R301.
8. Siegel, P.H., *Terahertz technology.* Microwave Theory and Techniques, IEEE Transactions on, 2002. **50**(3): p. 910-928.
9. Dougherty, J.P., G.D. Jubic, and J.W.L. Kiser. *Terahertz imaging of burned tissue*. 2007. San Jose, CA, USA: SPIE.
10. Taylor, Z.D., et al., *THz Medical Imaging: in vivo Hydration Sensing.* IEEE Tran. On THz Science and Technology, 2011. **1**(1).
11. Taylor, Z.D., et al. *Active THz medical imaging using broadband direct detection*. 2013.
12. Wallace, V.P., et al., *Terahertz pulsed imaging of basal cell carcinoma ex vivo and in vivo.* British Journal of Dermatology, 2004. **151**(2): p. 424-432.

13. Woodward, R.M., Wallace, Vincent P, Pye, Richard J, Cole, Bryan E, Arnone, Donald D, Linfield, Edmund H, Pepper, Michael, *Terahertz Pulse Imaging of ex vivo Basal Cell Carcinoma.* J Investig Dermatol, 2003. **120**(1): p. 72-78.

14. Taylor, Z.D., et al., *THz Medical Imaging: in vivo Hydration Sensing.* Terahertz Science and Technology, IEEE Transactions on, 2011. **1**(1): p. 201-219.

15. Arbab, M.H., et al. *Characterization of burn injuries using terahertz time-domain spectroscopy*. 2011. San Francisco, California, USA: SPIE.

16. Singh, R.S., et al. *Terahertz sensing of corneal hydration*. in *Engineering in Medicine and Biology Society (EMBC), 2010 Annual International Conference of the IEEE*. 2010.

17. Brown, E.R., *Fundamentals of Terrestrial Millimeter-Wave and THz Remote Sensing.* International Journal of High Speed Electronics and Systems, 2003. **13**(04): p. 995-1097.

18. Semenov, A., et al., *Application of Zero-Bias Quasi-Optical Schottky-Diode Detectors for Monitoring Short-Pulse and Weak Terahertz Radiation.* Electron Device Letters, IEEE, 2010. **31**(7): p. 674-676.

19. Hesler, J.L. and T.W. Crowe. *NEP and responsivity of THz zero-bias Schottky diode detectors*. in *Infrared and Millimeter Waves, 2007 and the 2007 15th International Conference on Terahertz Electronics. IRMMW-THz. Joint 32nd International Conference on*. 2007.

20. Han, P.Y. and X.-C. Zhang, *Free-space coherent broadband terahertz time-domain spectroscopy.* Measurement Science and Technology, 2001. **12**(11): p. 1747.

21. Liebe, H., G. Hufford, and T. Manabe, *A model for the complex permittivity of water at frequencies below 1 THz.* International Journal of Infrared and Millimeter Waves, 1991. **12**(7): p. 659-675.

22. Ronne, C., et al., *Investigation of the temperature dependence of dielectric relaxation in liquid water by THz reflection spectroscopy and molecular dynamics simulation.* The Journal of Chemical Physics, 1997. **107**(14): p. 5319-5331.

23. Yura, H.T. and T.S. Rose, *Gaussian beam transfer through hard-aperture optics.* Appl. Opt., 1995. **34**(30): p. 6826-6828.

24. Taylor, Z.D., *Active THz imaging for medical applications*. 2009, University of California, Santa Barbara: Ann Arbor. p. 210.

25. Malone, R.M., et al., *Design of a thermal imaging diagnostic using 90-degree, off-axis parabolic mirrors* Office of Scientific and Technical Information (OSTI), 2003.

26. Herloski, R., S. Marshall, and R. Antos, *Gaussian beam ray-equivalent modeling and optical design.* Appl. Opt., 1983. **22**(8): p. 1168-1174.

27. Jackson, T.J., *III. Measuring surface soil moisture using passive microwave remote sensing.* Hydrological Processes, 1993. **7**(2): p. 139-152.

28. Thorsos, E.I., *The validity of the Kirchhoff approximation for rough surface scattering using a Gaussian roughness spectrum.* The Journal of the Acoustical Society of America, 1988. **83**(1): p. 78-92.

29. Beckmann, P. and A. Spizzichino, *The Scattering of Electromagnetic Waves from Rough Surfaces.* 1963.

30. Piesiewicz, R., et al., *Scattering Analysis for the Modeling of THz Communication Systems.* Antennas and Propagation, IEEE Transactions on, 2007. **55**(11): p. 3002-3009.

31. Tchvialeva L., Z.H., Markhvida I., McLean D.I., Lui H. and Lee T.K., *Skin Roughness Assessment.* Recent Advances in Biomedical Engineering, 2010: p. 341-358.

32. Cook, T.H., et al., *Quantification of the skin's topography by skin profilometry*. International Journal of Cosmetic Science, 1982. **4**(5): p. 195-205.

33. Zimnyakov, D.A., et al. *Speckle pattern statistics analysis in human skin structure investigations*. 1994.

34. Goldsmith, P., *Gaussian Beam Quasioptical Propogation and Applications*. Quasioptical Systems. 1998, Piscataway, NJ: IEEE Press.